AD-A147 304 ACTA AERONAUTICA ET ASTRONAUTICA SINICA (SELECTED ARTICLES)(U) FOREIGN TECHNOLOGY DIV WRIGHT-PATTERSON AFB OH 04 OCT 84 FTD-ID(RS)T-1120-84 1/1

UNCLASSIFIED F/G 20/4 NL

END

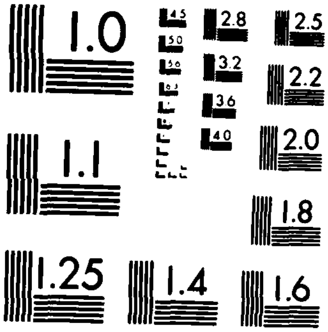

MICROCOPY RESOLUTION TEST CHART
NATIONAL BUREAU OF STANDARDS-1963-A

FTD-ID(RS)T-1120-84

FOREIGN TECHNOLOGY DIVISION

ACTA AERONAUTICA ET ASTRONAUTICA SINICA

(Selected Articles)

DTIC
ELECTE
NOV 9 1984
A

Approved for public release;
distribution unlimited.

FTD-ID(RS)T-1120-84

EDITED TRANSLATION

FTD-ID(RS)T-1120-84 4 October 1984

MICROFICHE NR: FTD-84-C-000974

ACTA AERONAUTICA ET ASTRONAUTICA SINICA
(Selected Articles)

English pages: 60

Source: Hangkong Xuebao, Vol. 4, Nr. 4, 1983,
pp. 1-10; 11-19; 39-47; 101-104

Country of origin: China
Translated by: LEO KANNER ASSOCIATES
F33657-81-D-0264
Requester: FTD/TQTA
Approved for public release; distribution unlimited.

PREPARED BY:

TRANSLATION DIVISION
FOREIGN TECHNOLOGY DIVISION
WP-AFB, OHIO.

FTD -ID(RS)T-1120-84 Date 4 Oct 1984

TABLE OF CONTENTS

A-1

GRAPHICS DISCLAIMER

SECOND ORDER APPROXIMATION METHOD FOR TRANSONIC FLOWS OVER SWEPT WINGS

Shen Keyang
Shanghai Aviation Industry Corporation

Abstract

This paper uses the TSDH equation to calculate the transonic flows over three-dimensional swept wings. It considers the leading edge boundary conditions and leading edge velocity potential equation suitable for the blunt leading edge of wings. We use the expanded form of the Jameson scheme in the unequal step length grid for the disretization of the TSDH equation into a set of finite difference equations. Afterwards, we arranged a rarefied grid in the calculation space, then arranged a dense grid near the wing and carried out alternate iteration of the rarefied and dense meshes so as to accelerate convergence and raise calculation precision. Calculations of the supercritical without shock wave and with shock wave conditions of the ONERA M6 wing show that there is good agreement between the TSDH solution and the FVP solution and wind tunnel tests.

Symbols

a : local velocity of sound
E : iteration error
M : Mach number
n : iteration number
a : attack angle
γ : specific heat ratio of air
δ : mean relative thickness of wing
ε : small disturbance parameters, $\varepsilon = \delta^{2/3}/M_\infty$
Λ : sweepback angle

Lower Symbols

∞ : free flow
LE : leading edge
TE : trailing edge

Upper Symbols

(n) : the n number iterations
x,y,z : right angle coordinate system, x axis along wing chord direction, the y axis goes up
Q : flow velocity
$y_w(x)$: wing configuration coordinate
μ : switch parameters
Φ : full velocity potential
φ : disturbance velocity potential
ω_d : damping coefficient
ω_p : low relaxation coefficient
u : upper wing surface
l : low wing surface.
(n-1) : the (n-1) number iterations

I. Introduction

Because of the simplicity of the calculations of the classical transonic small disturbance theory (TSD equation), it has continuously been given attention. However, when compared with the full velocity potential theory (FVP equation), it has the following two major drawbacks: (1) because a longitudinal disturbance velocity component is not designed into the wing surface's boundary conditions, infinitely great singularity is produced in the area of the blunt leading edge; (2) based on the conditions of the existence of shock waves on the infinite swept wing [1], the TSD equation is only suitable for situations wherein the wing's sweepback angle is relatively small (see Appendix A). People hope to attain a calculation method which will on the one hand maintain the simplicity of the TSD theory and can also overcome the two above mentioned drawbacks. Ballhaus and Bailey [1] used the MSD equation to basically overcome the above drawback (2) yet it does not consider drawback (1). In recent years, References [2,3] researched the second-order approximation method (TSDH equation) in the transonic small disturbance potential flow and its application for the flow over airfoil overcame the above drawback (1) and obtained results very close to the FVP solution. The aim of this paper is to extend this method to the transonic flow over three-dimensional wings and thus overcome the above drawbacks of the TSD equation and obtain results very close to the FVP solution.

In order to be able to be suitable for calculation of wings with complex configurations as well as wings having a fence, leading edge sawteeth or wingtip winglet etc. aerodynamic equipment, this paper does not carry out certain coordinate conversion of the TSDH equation but directly solves its difference equation in the physical space. At the same time, this paper uses Boppe's [4] rarefied and dense mesh alternate iteration method to raise the convergence speed and reduce the requirements for computer storage. Calculations of ONERA M6 wing with complex shock wave form show that the method in this paper is effective.

II. Basic Equations and their Boundary Conditions

Based on the research of References [2,3], the second-order and some of the third-order terms of the transonic small disturbance velocity potential equation (TSDH equation) retained in the three-dimensional situations can be expressed as follows:

$$\left[1-M_\infty^2-(\gamma+1)M_\infty^2\varepsilon\varphi_x-\mu\frac{\gamma+1}{2}M_\infty^2\varepsilon^2\varphi_x^2\right]\varphi_{xx}+[1-\mu(\gamma-1)M_\infty^2\varepsilon\varphi_x](\varphi_{yy}+\varphi_{zz})$$
$$-2\mu M_\infty^2(1+\varepsilon\varphi_x)[(\alpha+\varepsilon\varphi_y)\varphi_{xy}+\varepsilon\varphi_z\varphi_{xz}]=0 \qquad (1)$$

In the formula, μ =1 and when μ =0, formula (1) is simplified into the TSD equation. The wing surface's boundary conditions (except for the leading edge) can be expressed as

$$\varphi_y(x,\ \pm 0,\ z)=\varepsilon_1\left\{\left(\frac{\partial y_w}{\partial x}\right)_{u,l}[\cos\alpha+\mu\varepsilon\varphi_x(x,\ \pm 0,\ z)]-\sin\alpha\right\} \qquad (2)$$

In the formula, $\varepsilon_1=f_c/\varepsilon$, f_c is the correction coefficient and this paper uses $f_c=M_\infty^{1/4}$ (when $M_\infty \leqslant 1$). In the blunt leading edge $x=x_{LE}(z)$ area, $(\partial y_w/\partial x)_{u,l}=\infty$ and its leading edge boundary condition is

$$\varphi_{x_{LE}}=\varphi_{z_{LE}}\operatorname{tg}\Lambda_{LE}-\frac{\cos\alpha}{\varepsilon} \qquad (3)$$

We substitute formula (3) into the FVP equation

$$(a^2-\Phi_x^2)\varphi_{xx}+(a^2-\Phi_y^2)\varphi_{yy}+(a^2-\Phi_z^2)\varphi_{zz}-2\Phi_x\Phi_y\varphi_{xy}-2\Phi_x\Phi_z\varphi_{xz}-2\Phi_y\Phi_z\varphi_{yz}=0 \qquad (4)$$

The obtainable simplified FVP equation of the wing's blunt leading edge is

$$\left[1-\left(\frac{\operatorname{tg}\Lambda_{LE}\varepsilon\varphi_{z_{LE}}}{a^*}\right)^2\right]\varphi_{xx}+\left[1-\left(\frac{\varepsilon\varphi_{y_{LE}}+\sin\alpha}{a^*}\right)^2\right]\varphi_{yy}+\left[1-\left(\frac{\varepsilon\varphi_{z_{LE}}}{a^*}\right)^2\right]\varphi_{zz}$$
$$-2\operatorname{tg}\Lambda_{LE}\left(\frac{\varepsilon\varphi_{z_{LE}}}{a^*}\right)^2\varphi_{xz}-2\operatorname{tg}\Lambda_{LE}\left[\frac{\varepsilon\varphi_{z_{LE}}(\varepsilon\varphi_{y_{LE}}+\sin\alpha)}{a^{*2}}\right]\varphi_{xy}$$
$$-2\frac{\varepsilon\varphi_{z_{LE}}(\varepsilon\varphi_{y_{LE}}+\sin\alpha)}{a^{*2}}\varphi_{yz}=0 \qquad (5)$$

In the formula

$$a^{*2}=\frac{a_{LE}^2}{Q_\infty^2}=M_\infty^{-2}+\frac{\gamma-1}{2}\left[1-\left(\frac{\varepsilon\varphi_{z_{LE}}}{\cos\Lambda_{LE}}\right)^2-(\varepsilon\varphi_{y_{LE}}+\sin\alpha)^2\right] \qquad (6)$$

Because we only consider the longitudinal flow, there are symmetric conditions on the wing's central line

$$\varphi_z=\varphi_{zz}=0 \qquad (7)$$

The sweepback discontinuity surface conditions and distant field boundary conditions of the wing are identical to those in Reference [5]. Wing surface pressure coefficient Cp is calculated with the Bernoulli equation:

$$C_p=\frac{2}{\gamma M_\infty^2}\left[\left\{1-\frac{\gamma-1}{2}M_\infty^2[2\varepsilon\varphi_x+\varepsilon^2\varphi_x^2+\mu(2\alpha\varepsilon\varphi_y+\varepsilon^2\varphi_y^2+\varepsilon^2\varphi_z^2)]\right\}^{\gamma/(\gamma-1)}-1\right] \qquad (8)$$

III. The Finite Diffference Form and Solution Equation

Based on the discussion in Reference [3] regarding numerical calculation stability and artificial viscosity directionality, formula (1) only has φ_{xx} which should based on the changes of the equation form use the central difference or upstream difference form and each of the rest of the terms then always use the central difference form. Therefore, the difference form of this method is non-rotational and the calculations are simpler than those of the full velocity potential equation. We use the extended form of the Jameson scheme in a non-uniform grid. For example, in supersonic points (i,j,k), we can change formula (1) into

$$\begin{aligned}
&2F_{xx\,i,j,k}^{(n-1)}\left[\frac{\tilde{\varphi}_{i,j,k}^{(n)}}{pq}-\frac{\varphi_{i-1,j,k}^{(n)}}{pq}-\frac{\varphi_{i,j,k}^{(n-1)}}{p(p+q)}+\frac{\varphi_{i-2,j,k}^{(n-1)}}{p(p+q)}\right]\\
&+2F_{yz\,i,j,k}^{(n-1)}\left[\frac{\tilde{\varphi}_{i,j+1,k}^{(n)}}{n(m+n)}-\frac{\tilde{\varphi}_{i,j,k}^{(n)}}{mn}+\frac{\tilde{\varphi}_{i,j-1,k}^{(n)}}{m(m+n)}\right]\\
&+2F_{yz\,i,j,k}^{(n-1)}\left[\frac{\varphi_{i,j,k+1}^{(n-1)}}{v(u+v)}-\frac{\varphi_{i,j,k}^{(n-1)}}{v(u+v)}-\frac{\tilde{\varphi}_{i,j,k}^{(n)}}{u(u+v)}+\frac{\varphi_{i,j,k-1}^{(n)}}{u(u+v)}\right]\\
&-2\mu M_\infty^2(1+\varepsilon\varphi_{x\,i,j,k}^{(n-1)})[(\alpha+\varepsilon\varphi_{y\,i,j,k}^{(n-1)})\varphi_{xy\,i,j,k}^{(n)}+\varepsilon\varphi_{z\,i,j,k}^{(n-1)}\varphi_{xz\,i,j,k}^{(n)}]\\
&-\frac{2\omega_d\sqrt{M_{i,j,k}^2-1}}{q(q+r)}(\tilde{\varphi}_{i,j,k}^{(n)}-\varphi_{i-1,j,k}^{(n)}-\varphi_{i,j,k}^{(n-1)}+\varphi_{i-1,j,k}^{(n-1)})=0 \qquad (9)
\end{aligned}$$

In the formula, we take $\omega_d \geqslant 0$, $p=x_{i-1}-x_{i-2}$, $q=x_i-x_{i-1}$,

$r=x_{i+1}-x_i$, $m=y_j-y_{j-1}$, $n=y_{j+1}-y_j$, $u=z_k-z_{k-1}$, $v=z_{k+1}-z_k$ as well as

$$F^{(n-1)}_{x_{s\,i,j,k}}=1-M_\infty^2-(\gamma+1)M_\infty^2\varepsilon\varphi^{(n-1)}_{x_{s\,i,j,k}}-\mu\frac{\gamma+1}{2}M_\infty^2\varepsilon^2[\varphi^{(n-1)}_{x_{s\,i,j,k}}]^2$$

In the formula, $\varphi_{x_{s\,i,j,k}}^{(n-1)}$ is calculated by the upstream difference formula,

$$F^{(n-1)}_{yz_{i,j,k}}=1-\mu(\gamma-1)M_\infty^2\varepsilon\varphi^{(n-1)}_{x_{i,j,k}}$$

$$\varphi^{(n)}_{xy_{i,j,k}}=\frac{1}{(q+r)(m+n)}[\varphi^{(n-1)}_{i+1,j+1,k}-\varphi^{(n-1)}_{i+1,j-1,k}-\varphi^{(n)}_{i-1,j+1,k}+\varphi^{(n)}_{i-1,j-1,k}]$$

$$\varphi^{(n)}_{xz_{i,j,k}}=\frac{1}{(q+r)(u+v)}[\varphi^{(n-1)}_{i+1,j,k+1}-\varphi^{(n-1)}_{i+1,j,k-1}-\varphi^{(n)}_{i-1,j,k+1}+\varphi^{(n)}_{i-1,j,k-1}]$$

In the formula, $\varphi_z^{(n-1)}$ as well as $\varphi_y^{(n-1)}$ and $\varphi_z^{(n-1)}$ are all calculated by the central difference formula. After solving $\tilde{\varphi}^{(n)}_{i,j,k}$ by the set of difference equations, we can use the following formula to obtain $\varphi^{(n)}_{i,j,k}$

$$\varphi^{(n)}_{i,j,k}=\varphi^{(n-1)}_{i,j,k}+\omega_p(\tilde{\varphi}^{(n)}_{i,j,k}-\varphi^{(n-1)}_{i,j,k}) \qquad (10)$$

In the formula, we take $\omega_p \leqslant 1$.

For each term in leading edge equation (5), φ_{xx}, φ_{xy} and φ_{zz} use a one-sided difference formula to satisfy the boundary conditions of formula (3) and φ_{yy} and φ_{zz} then use the central difference formula. Moreover, only when $\mu=1$ can formula (5) participate in the operation and combine with formula (1) for solution.

When solving velocity potential φ, we arrange two grids in the calculating space: we arrange a rarefied mesh in the calculating space (for example, 30x21x15, at this time the spanwise direction of the wing surface is cut into several sections and each section has 5-7 chordwise mesh points) and at the same time we arrange a dense mesh near the wing (the density of the dense mesh is fixed in view of requirements, the most rarefied situation is 35x25x15 and at this time the spanwise direction of the wing surface is cut into more than ten sections and each section has 15-20 chordwise mesh points). Afterwards, we carry out rarefied and dense mesh alternate iteration. The solution process is carried out in three stages:

The first stage: we give a velocity potential initial field in the rarefied mesh, for example, we take $\varphi^{(0)}_{i,j,k}=0$. Taking $\mu=0$, we carry out iteration solution of equations (1) and and at the same time continuously change the distant field velocity potential with the increase of the circulation. Because the grid is relatively rarefied, after a relatively small number of iterations, it can reach convergence standard $E=MAX|\varphi^{(n)}-\varphi^{(n-1)}|\leqslant 10^{-2}-10^{-3}$. In this way, we establish the approximate velocity potential field and circulation distribution in the entire calculating space.

The second stage: this stage is carried out in two steps. The first step is finding the initial field of the dense mesh velocity potential from the rarefied mesh velocity potential interpolation. For the velocity potential value of the fixed dense mesh's outer boundary, we carry out iteration solution using $\mu=0$ in a dense mesh for formulas (1) and (2) so as to attain convergence standard $E\leqslant 10^{-3}-10^{-4}$. The second step is to find the velocity potential value on the wing surface in the rarefied mesh from the dense mesh's velocity potential interpolation found in the first step, to find the rarefied mesh's distant field velocity potential value from the dense mesh's circulation distribution and the two remain unchanged during the iteration process. Therefore, this step solves the rarefied mesh's velocity potential under Dirichlet boundary conditions.

At this time, we still use $\mu=0$ and after attaining the convergence standard we again repeat the first step. After alternate iteration of the rarefied and dense meshes and the wing surface pressure coefficient in the dense mesh reaches a certain convergence standard, we can conclude the operation of the second step.

The third step is carrying out densification of the dense mesh so as to attain the number of mesh points sufficient for the needs of the wing. At this time, the velocity potential value of the fixed dense mesh's outer boundary uses $\mu=1$ for the iteration solutions of formulas (1) and (2). At the same time, calculated leading adge equation (5) and leading edge boundary conditions (3) thus obtain the finally needed calculation results.

We can see from this that the main calculation quantities are carried out by the TSD equation and only in the final stage do we use the TSDH equation and leading edge equation. Therefore, the calculation method in this paper is much simpler than directly solving the FVP equation.

IV. Calculation Results and Discussion

We used the above mentioned method to calculate the pressure distribution of the ONERA M6 wing under two types of situations. The leading edge sweepback angle of this wing is 30° and the aspect ratio and taper ratio are 3.8 and 0.562, respectively. Since this wing has a pointed D airfoil section, the form of its pressure distribution is rather complex and under certain flow conditions it has a complex shock wave form. Therefore, this wing has become the standard model for testing transonic calc methods.

Figure 1 shows the TSDH solution for sectional pressures at two span wise stations under supercritical conditions with no shock wave when $M_\infty = 0.70$ and $\alpha = 3^\circ$, and it is very close to the wind tunnel tests (7) and FVP solutions (8).

Figure 2 gives the section pressure distribution ~~on~~ at six spanwise positions when M_∞ =0.84 and a=3.06° and it is compared with the test values [7] and FVP solution [[illegible]]. We can see from the figure that the TSDH solution is very close to the test values and FVP solution and relatively well reflects the complex shock wave form on the wing surface. On a section with z=80%, the TSDH solution is even closer to the test values as compared to the FVP solution. In the z=95% area, the TSDH solution has a certain difference with the test values and the main reason is there is no further division of the grid between z=95% and the wing tip and this affects the accuracy of the results. The figure always gives the TSD solution with μ=0 and comparison with the TSDH solution shows that the level of congruence between the TSD solution and test values is relatively poor and cannot very well reflect the complex shock wave form on the wing. Figure 3 gives the shock wave position on the M6 wing when M_∞ =0.84 and a=3.06° and it can be seen that the TSDH solution is very close to the test values. After z $\geqslant$ 80%, the calculated positive shock wave position is more towards the front than the test values and this is because the spanwise grid near the wingtip is very rarefied. Therefore, in order to attain accurate results it is necessary to guarantee the density of the grid. When calculated in a situation wherein M_∞ =0.84, in order to approximately consider the disturbance of the shock wave and boundary layer, we used the non-conservation shock wave point difference scheme [3]. Figure 4 further shows the necessity of guaranteeing the grid density. It can be seen from the figure that when the number of mesh points on the chord line is 53, the wing surface then has a leading edge suction peak and at the same time the shock wave position is clearly reflected. Therefore, when calculating the transonic pressure distribution of the wing surface, it is necessary to give sufficient attention to the grid density on the wing surface otherwise this can seriously influence the accuracy of the calculation results. Lastly, Fig. 5 shows the situation wherein when the TSDH equation and leading edge equation (5) are jointly solved, iteration error E changes with iteration number n. It can be seen from the figure that low relaxation coefficient ω_p has very good effects for quickening the convergence speed.

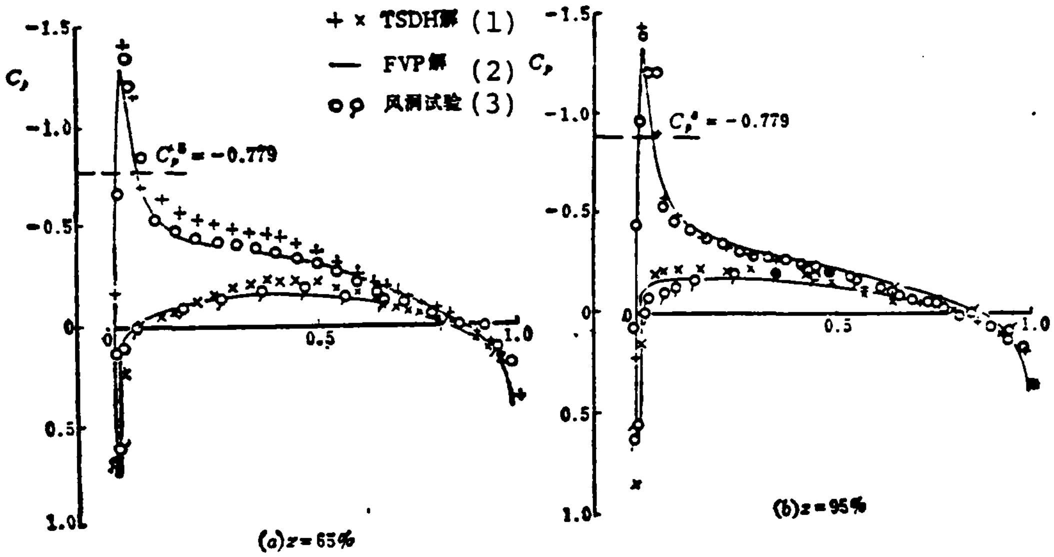

(a) z=65%

(b) z=95%

Fig. 1 Comparisons of pressure distributions and wind tunnel tests for M6 wing when M_∞ =0.70 and a=3°.
Key: (1)-(2) Solution; (3) Wind tunnel test.

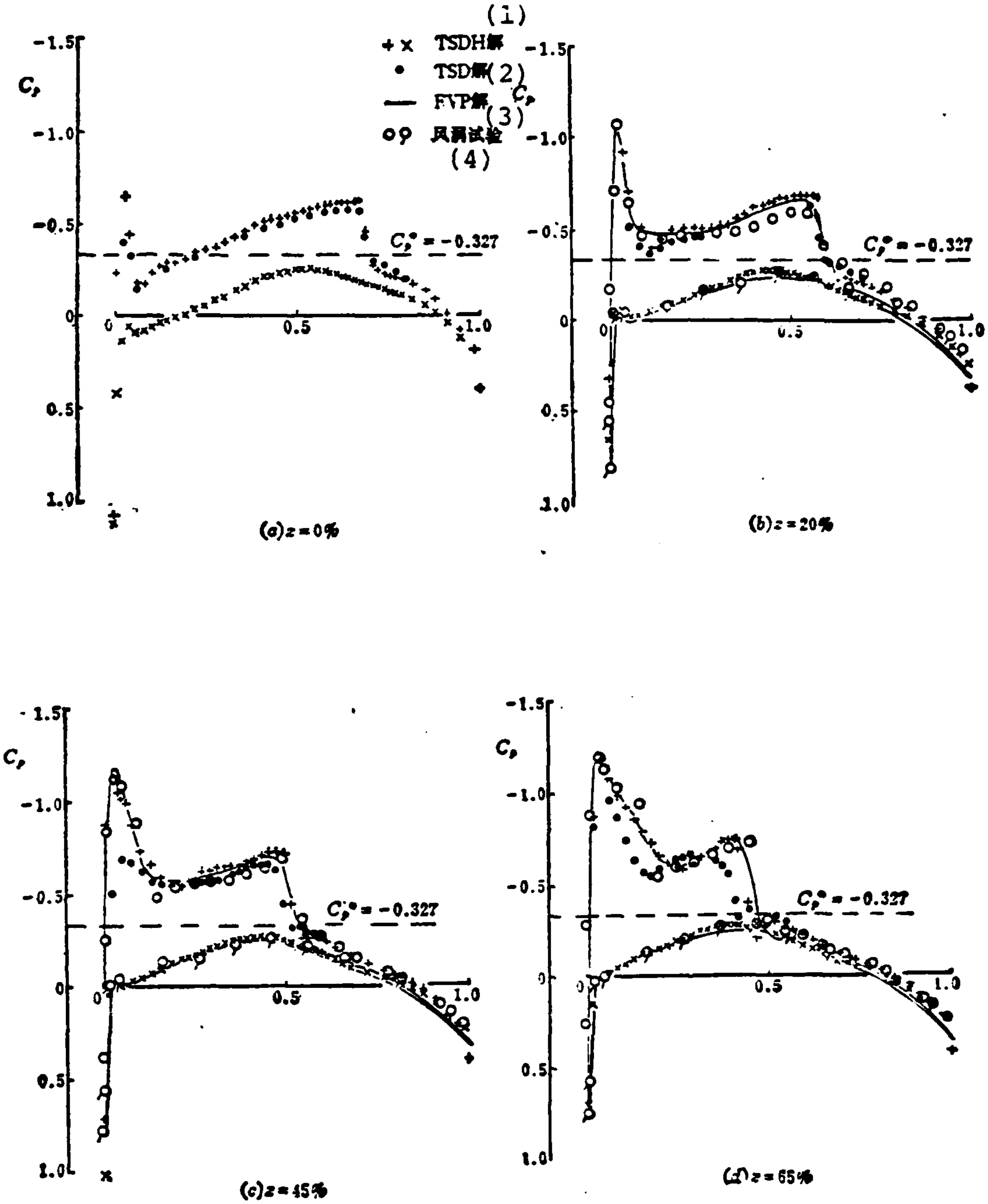

Fig. 2 (continued on next page)

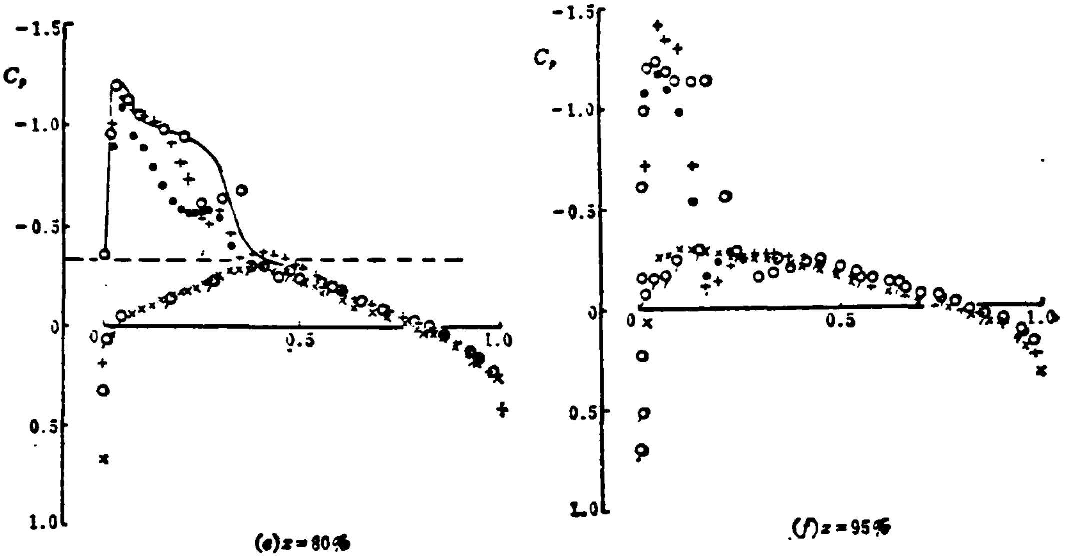

(e)z=80%

(f)z=95%

Fig. 2 Comparisons of pressure distributions and wind tunnel tests for M6 wing when M_∞ =0.84 and a=3.06°.
Key: (1)-(3) Solution; (4) Wind tunnel test.

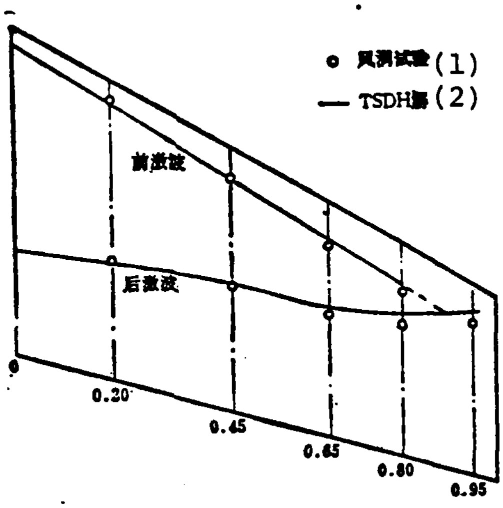

Fig. 3 Comparison of shock wave positions of M6 wing when M_∞ =0.84 and a=3.06°.
Key: (1) Wind tunnel test; (2) TSDH solution.

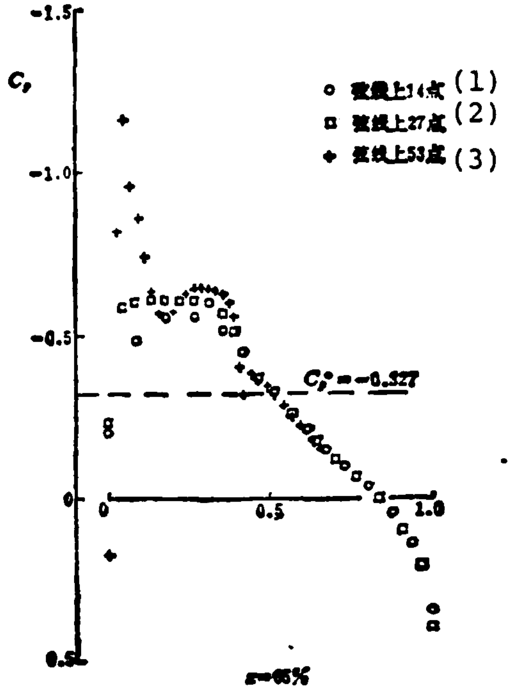

Fig. 4 Influence of grid density on chordwise pressure distribution results (TSDH solution) for M6 wing when M_∞ =0.84 and a=3.06°.

Key: (1) 14 points on chord line; (2) 27 points on chord line; (3) 53 points on chord line.

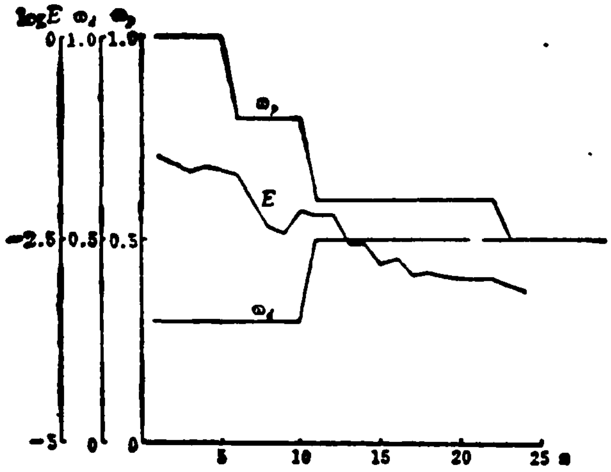

Fig. 5 Convergence behavior of TSDH solution (using the TSD solution as the initial field) for the M6 wing when M_∞ =0.84 and a=3.06°.

V. Conclusion

The TSDH equation and simplified leading edge equation as well as its corresponding boundary conditions in the three-dimensional flow used in this paper can relatively well attain the transonic pressure distribution of the wing and can relatively well reflect the complex shock wave form on the wing. Because the TSD equation does not consider the cross derivative of the velocity potential, its calculation accuracy is relatively poor. Because this paper does not carry out coordinate conversion, it can therefore conveniently consider the complex configuration of the wing as well as the fence, leading edge sawteeth and wingtip winglet etc. aerodynamic equipment on the wing surface; however, the nonadvantageous factors follow the densification of the chordwise division points and it is necessary to correspondingly and suitably increase the number of chordwise division points otherwise it easily causes fluctuation of the calculation results of the separate points near the leading edge.

This research work received the enthusiastic attention and guidance of Professor Luo Shijun and we would like to thank him here.

Appendix A Conditions of Shock Waves Existing on an Infinite Swept Wing

Reference [1] discussed the conditions of shock waves existing on an infinite swept wing. If the sweepback angle of the shock wave or leading edge of the wing is Λ , then the conditions of the existing sweepback shock waves, which is the velocity component of the shock wave normal line direction on the wing plane, must be greater than the local velocity of sound. It can be expressed as

$$\Phi_{\hat{x}} > \Phi^{*}_{\hat{x}} = a \qquad \text{(A1)}$$

In the formula, $\hat{x}$ is the chordwise coordinate of the infinite swept wing (see Fig. A-1).

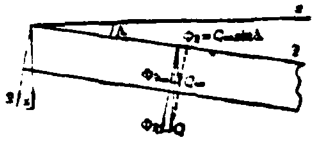

Fig. A-1 Coordinate direction of infinite swept wing.

Because the flow component does not change along the z axis, formula (A1) can be rewritten as

$$\phi_x < \phi_x^* < (\phi_x)_{\max} \qquad \text{(A2)}$$

In the formula, $\Phi_x = \varepsilon \varphi_{xo}$ and $(\Phi_x)_{\max}$ corresponds to the maximum value of a=0. From the energy equation, we can obtain

$$(\phi_x)_{\max} = -\cos^2\Lambda\left[1-\sqrt{1+\frac{2}{\gamma-1}(M_\infty^2\cos^2\Lambda)^{-1}}\right] \qquad \text{(A3)}$$

Assuming $\Phi_y=0$, we can obtain different Φ_x^* expressions for the different velocity potential equations. For the FVP equation

$$\phi_x^* = -\cos^2\Lambda\left\{1-\sqrt{1-\frac{2}{\gamma+1}[1-(M_\infty^2\cos^2\Lambda)^{-1}]}\right\} \qquad \text{(A4)}$$

For the TSD equation

$$\phi_x^* = \frac{\sec^2\Lambda - M_\infty^2}{(\gamma+1)M_\infty^2} \qquad \text{(A5)}$$

For the TSDH equation

$$\phi_x^* = [\sqrt{B_4^2 - 2A_4(M_\infty^2 - \sec^2\Lambda)} - B_4]/A_4 \qquad \text{(A6)}$$

In the formula

$$A_4 = (\gamma+1)M_\infty^2 + 4M_\infty^2\mathrm{tg}^2\Lambda$$
$$B_4 = (\gamma+1)M_\infty^2\sec^2\Lambda$$

For the longitudinal large disturbance velocity potential equation [5]

$$\phi_x^* = \sqrt{1 - \frac{2(M_\infty^2 - \sec^2\Lambda)}{A_s}} - 1 \qquad \text{(A7)}$$

In the formula

$$A_s = (\gamma + 1)M_\infty^2 + (\gamma - 1)M_\infty^2 \mathrm{tg}^2\Lambda$$

Figure A-2 gives the relationship of the Φ_x^* obtained from formulas (A4)-(A7) when M_∞ =0.85 which changes with sweepback angle Λ. It can be seen from the figure that for an infinite swept wing with $\Lambda > 50°$, the TSD equation is unable to obtain shock waves, the longitudinal large disturbance equation causes Λ to increase to 60° and the TSDH equation causes Λ to increase to 80°.

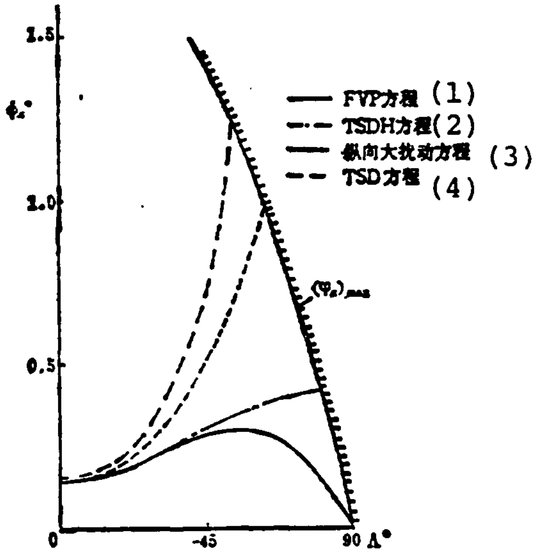

Fig. A-2 Conditions of existence of shock waves on infinite swept wing $\Phi_x^* < \Phi_x < (\Phi_x)_{max}$ for M_∞ =0.85.

Key: (1)-(2) Equation; (3) Longitudinal large disturbance equation; (4) Equation.

References

[1] W.F. Ballhaus, F.R. Bailey and J. Frick, Improved computational treatment of transonic flows about swept wings, NASA CP-2001 (1976) 1311-1320.

[2] Shen Keyang, Transonic second order small disturbance velocity potential equation and its difference calculation, Shanghai Mechanics, Vol. 2, No. 2 (1981), 31-42.

[3] Shen Keyang and Luo Shijun, Second order approximate method for transonic small disturbance potential flow and its application to analysis of flows over airfoils, to be published in Computer Methods in Applied Mechanics and Engineering.

[4] C.W. Boppe, Calculation of transonic wing flows by grid embedding, AIAA paper 77-207.

[5] Luo Shijun et al, Mixed difference method of transonic constant potential flow, National Defense Insustry Press, 1979.

[6] V. Schmitt and F. Manie, Ecoulement subsoniques et transoniques sur une aile a fleche variable, La Recherche Aerospatiale, 1979-4, 219-237.

[7] B. Monnerie and F. Charpin, Essais de buffeting d'une aile en fleche en transsonique, 10 Colloque D'Aerodynamique Appliquee (1973).

[8] J.J. Chattot et al, Calculs d'ecoulements transsoniques autour d'ailes, La Recherche Aerospatiale, 1978-4, 143-159.

[9] A. Jameson and D.A. Caughey, A finite volume method for transonic potential flow calculations, AIAA 77-635.

A NUMERICAL SOLUTION OF THE SHOCK-TURBULENT INTERACTION OVER A COMPRESSION CORNER FOR SUPERSONIC FLOW

Cao Qipeng

Nanjing Aeronautical Institute

Abstract

This paper calculates the shock-turbulent boundary layer interaction over a compression corner for supersonic flow. The calculations use the Cebeci-Kellet Box method; the turbulence model uses the algebraic eddy viscosity model; the pressure strength distribution uses the unified hypersonic and supersonic formulas of flowing over a wedge; we carry out iteration correction of the shock-turbulent boundary layer disturbance. The calculations predict the wall pressure distribution as well as the initial rise point location of the pressure.

I. Introduction

The compression corner for supersonic flow is a classical example of interference between the shock wave and boundary layer. The turbulent flow especially has even more real significance. It is related to the operating efficiency when an aircraft deflects the operating surface and it is also related to supersonic inlet surge. Thus, it has consistently been an important problem which has gained a great deal of attention in aerodynamic design.

Early, in the 1950's, Drougge et al [1,2,3,4] carried out experimental research on the problem of disturbence between the shock wave and boundary layer produced by the supersonic flow over a compression corner. The earliest theoretical calculations used the boundary layer momentum integral relation method and it was quite rough. For improvement, in the 1970's, they began using a succession of methods [5,6] and at the same time following the advances in aerodynamic numerical calculations, two other calculation methods appeared. One type used the finite difference method to solve the boundary differential equation, carried out iteration coupling with external inviscid flow [7] or carried out boundary layer inverse problem solution of the disturbance region [8]. This method separately solves non-separated and separated flows and when compared with another method of directly numerically solving the Reynold's mean Navier-Stokes equation [9,10,11], the calculation accuracy is a little poorer especially for separated flows where it is necessary to make large improvements. However, it has a small amount of calculations, it saves on computer time and it is even more suitable for the present level of China's computers. This paper uses the first type of method under these assumptions yet uses the Cebeci-Keller Box method for solution of the equation, the further simplification of calculations and the saving of computer time. Accuracy is relatively good.

II. The Cebeci-Keller Box Solution Method For Binary Constant Compressible Turbulent Flow Boundary Layer Equations

1. Equations and Conversions

The set of binary constant compressible turbulent flow boundary layer equations are

Continuous

$$\frac{\partial}{\partial x}(\bar{\rho}\bar{u})+\frac{\partial}{\partial y}(\bar{\rho}\bar{v})=0 \qquad (1)$$

Momentum

$$\bar{\rho}\bar{u}\frac{\partial\bar{u}}{\partial x}+\bar{\rho}\bar{v}\frac{\partial\bar{u}}{\partial y}=-\frac{d\bar{p}}{dx}+\frac{\partial}{\partial y}\left(\bar{\mu}\frac{\partial\bar{u}}{\partial y}-\bar{\rho}\overline{u'v'}\right) \qquad (2)$$

Energy

$$\bar{\rho}\bar{u}\frac{\partial\bar{H}}{\partial x}+\bar{\rho}\bar{v}\frac{\partial\bar{H}}{\partial y}=\frac{\partial}{\partial y}\left[\bar{\mu}\left(1-\frac{1}{P_r}\right)\bar{u}\frac{\partial\bar{u}}{\partial y}+\frac{\bar{\mu}}{P_r}\frac{\partial\bar{H}}{\partial y}-\bar{\rho}\overline{v'}\overline{H'}\right] \qquad (3)$$

In the formula, $-\overline{\rho}\ \overline{u'}\ \overline{v'} = \tau_t$ is called the Reynold's stress and based on the Boussinesq eddy viscosity formula it can be written as:

$$\tau_t = \varepsilon_t \frac{\partial \bar{u}}{\partial y},\ \varepsilon_t\text{为涡粘性系数}\ (1)$$

Key: (1) Is the eddy viscosity coefficient.

In the same way, $-\rho\ \overline{v'}\ \overline{H'} = \frac{\varepsilon_t}{Pr_t}\ \frac{\partial \bar{H}}{\partial y}$, Pr_t is the turbulent flow Prandtl number which this paper takes as 0.9; Pr is the molecular Prandtl number which this paper takes as 0.72. $\bar{H}$ represents the total enthalpy, $\bar{H} = \frac{\bar{u}^2}{2} + h$, h represents the static enthalpy; the "-" above each physical quantity indicates the mean number and u', v' and H' indicate the pulsation values of the velocity and total enthalpy.

The boundary conditions are:

$$\bar{u}(x,0)=0,\ \bar{v}(x,0)=0,\ \lim_{y\to\infty}\bar{u}(x,y)=u_e(x)$$

$$\bar{H}(x,0)=\bar{H}_w\ \overset{(1)}{\text{或}}\ \left.\frac{\partial \bar{H}}{\partial y}\right|_{y=0} = \left(\frac{\partial \bar{H}}{\partial y}\right)_w \qquad (4)$$

Key: (1) Or.

Lower symbol w indicates the wall surface value; e indicates the boundary layer's peripheral value.

We carry out conversion of the above set of equations and let

$$\xi = x, \qquad d\eta = \left(\frac{u_e}{\rho_e \mu_e x}\right)^{1/2} \bar{\rho}\, dy \qquad (5)$$

From the continuity equation we can introduce the flow function

$$\psi = (\rho_e \mu_e u_e x)^{1/2} f(\xi,\ \eta)$$
$$\bar{u} = u_e f' \qquad (6)$$

Substituting in formulas (2) and (3), after arrangement and obtaining conversion the equations are:

Momentum

$$(bf'')' + P_1 ff'' + P_2\left(\frac{\rho_e}{\rho} - f'^2\right) = \xi\left(f'\frac{\partial f'}{\partial \xi} - f''\frac{\partial f}{\partial \xi}\right) \qquad (7)$$

Energy

$$(es' + df'f'')' + P_1 fs' = \left(f'\frac{\partial s}{\partial \xi} - s'\frac{\partial f}{\partial \xi}\right) \qquad (8)$$

In the formulas

$$s = \bar{H}/H_e, \quad b = c\,(1 + \varepsilon_m/\bar{\nu}), \quad c = \bar{\rho}\bar{\mu}/\rho_e\mu_e,$$
$$\varepsilon_m = \varepsilon_t/\rho, \quad \bar{\nu} = \bar{\mu}/\bar{\rho}$$
$$P_2 = \frac{x}{u_e}\frac{du_e}{dx}, \qquad P_1 = \frac{1}{2}\left[1 + P_2 + \frac{x}{\rho_e\mu_e}\frac{d}{dx}(\rho_e\mu_e)\right]$$
$$e = \frac{c}{P_r}\left(1 + \frac{\varepsilon_m}{\bar{\nu}}\frac{P_r}{P_{r_t}}\right), \quad d = c\,\frac{u_e^2}{H_e}\left(1 - \frac{1}{P_r}\right)$$

The sign carrying a'η 'indicates the derivative of η.

The boundary condition conversions are:

$$\begin{aligned} &\eta = 0, \; f' = 0, \; f = 0, \; s = s_w = \bar{H}_w/H_e \text{或} s' = s'_w \\ &\eta \to \infty, \; \lim_{\eta\to\infty} f' = 1, \; \lim_{\eta\to\infty} s = 1 \qquad (1) \end{aligned} \qquad (9)$$

Key: (1) Or.

Formulas (7) and (8) above which solved the velocity distribution and enthalpy distribution (or temperature distribution) in the boundary layer also necessitates the addition of relational formulas for the $\bar{\mu}$, $\bar{\rho}$ and ε_m distributions in the boundary layer. Here, the viscosity coefficient uses the Sutherland formula

$$\bar{\mu}=\beta\frac{\bar{T}^{3/2}}{\bar{T}+110.4}\text{公斤·秒/米}^2\ (1) \qquad (10)$$

$$\beta=1.458\times10^{-6}/9.80665\text{公斤·秒/米}^2\cdot K^{1/2}$$

(2)

Key: (1) Kg·seconds/m^2; (2) Kg·seconds/m^2.

We use state equation $\bar{p}=\bar{\rho}R\bar{T}$ to find the density equation:

Because of the $\frac{\partial\bar{p}}{\partial y}=\frac{\partial\bar{p}}{\partial\eta}\frac{\partial\eta}{\partial y}=0$, therefore the above formula can be changed to

$$p_e=\bar{\rho}R\bar{T} \qquad (11)$$

We use the Cebeci algebraic eddy viscosity model to find ε_m, that is, on the inner layer of the boundary layer:

$$(\varepsilon_m)_i=l^2\left|\frac{\partial\bar{u}}{\partial y}\right|$$

$$=0.16\nu_e Re_x^{1/2}\left(\int_0^\eta\frac{\rho_e}{\bar{\rho}}d\eta\right)^2\left[1-\exp\left(-\frac{x}{A}Re_x^{-1/2}\int_0^\eta\frac{\rho_e}{\bar{\rho}}d\eta\right)\right]^2 f'' \qquad (12a)$$

In the formula, mixing length l=ky[1-exp(-y/A)]

$$k=0.4$$

$$A=\frac{26}{N}\bar{\nu}\left(\frac{\bar{\tau}_w}{\bar{\rho}_w}\right)^{-1/2}\left(\frac{\bar{\rho}}{\bar{\rho}_w}\right)^{1/2}$$

$$\bar{\tau}_w=\bar{\mu}\left(\frac{\partial\bar{u}}{\partial y}\right)_{y=0}=\bar{\mu}_w u_e f''_w\left(\frac{u_e}{\rho_e\mu_e x}\right)^{1/2}\bar{\rho}_w$$

$$N=\left[1-11.8\left(\frac{\bar{\mu}_w}{\mu_e}\right)\left(\frac{\rho_e}{\bar{\rho}_w}\right)^2 P^+\right]^{1/2}$$

$$P^+=\frac{\nu_e u_e}{u_\tau^3}\frac{du_e}{dx} \qquad u_\tau=\sqrt{\bar{\tau}_w/\bar{\rho}_w}$$

On the outer layer of the boundary layer:

$$(\varepsilon_m)_o=0.0168\int_0^\infty(u_e-u)dy=0.0168\nu_e Re_x^{1/2}\int_0^\infty(1-f')\frac{\rho_e}{\bar{\rho}}d\eta \qquad (12b)$$

$$\nu_e=\mu_e/\rho_e$$

2. The Cebeci-Keller Box Solution Method [12,13]

A. We introduce a new variable and change formulas (7) and (8) into a set of five first order nonlinear equations. Letting

$$g = f' \tag{13}$$

$$w = g' \tag{14}$$

$$t = s' \tag{15}$$

then formulas (7) and (8) change into

$$(bw)' + P_1 fw + P_2\left[\frac{\rho_e}{\rho} - g^2\right] = \xi\left(g\frac{\partial g}{\partial \xi} - w\frac{\partial f}{\partial \xi}\right) \tag{16}$$

$$(et + dgw)' + P_1 ft = \xi\left(g\frac{\partial s}{\partial \xi} - t\frac{\partial f}{\partial \xi}\right) \tag{17}$$

The boundary conditions are:

$$\begin{aligned} &\eta = 0: \ f_w = 0,\ g_w = 0,\ s = s_w \underset{(1)}{\text{或}} s'_w = t_w \\ &\eta = \eta_\infty: \ g = 1,\ s = 1 \end{aligned} \tag{18}$$

Key: (1) Or.

B. Difference Equations

When using the difference for solution, the grid layout is

$$\begin{gathered} \xi_0 = 0,\ \xi_n = \xi_{n-1} + K_n,\quad n = 1, 2, \cdots\cdots, N \\ \eta_0 = 0, \eta_j = \eta_{j-1} + h_j,\quad j = 1, 2, \cdots\cdots, J \\ \eta_J = \eta_\infty \end{gathered}$$

In order to make the near wall grid dense and distant wall grid rarefied so as to suit the needs of boundary layer calculations and not cause an increase in the number of η direction grid points, we used

$$\begin{gathered} h_j = mh_{j-1},\quad m > 1 \\ \eta_j = h_1\frac{m^j - 1}{m - 1},\quad j = 1, 2, \cdots\cdots, J \end{gathered}$$

We consider that formulas (13), (14) and (15) do not contain x direction derivatives and therefore the η direction derivative uses the central difference of the nodal point (ξ n, $\eta_{j-1/2}$) in the ξn station area. The function value of the nodal point uses the mean value in the two top and bottom points and thus the three difference equations are

$$h_j^{-1}(f_j^n - f_{j-1}^n) = g_{j-1/2}^n = \frac{g_{j-1}^n + g_j^n}{2} \tag{19}$$

$$h_j^{-1}(g_j^n - g_{j-1}^n) = w_{j-1/2}^n = \frac{w_{j-1}^n + w_j^n}{2} \tag{20}$$

$$h_j^{-1}(s_j^n - s_{j-1}^n) = t_{j-1/2}^n = \frac{t_{j-1}^n + t_j^n}{2} \tag{21}$$

In the formulas, f_j^n indicates the f value of the η_j area in the ξ n station area and the remaining are analogously deduced.

Formulas (16) and (17) possess η direction derivatives and therefore the derivatives are replaced with the central difference of the central point ($\xi_{n-1/2}$, $\eta_{j-1/2}$) and the function value uses the mean value of the four points near the central point, that is, the difference equations are:

$$\begin{aligned} h_j^{-1}[(bw)_j^{n-1/2} - (bw)_{j-1}^{n-1/2}] &= -(P_1)_{n-1/2}(fw)_{j-1/2}^{n-1/2} - (P_2)_{n-1/2}\left[\left(\frac{\rho_e}{\bar{\rho}}\right)_{j-1/2}^{n-1/2} - (g^2)_{j-1/2}^{n-1/2}\right] \\ &\quad + \xi_{n-1/2}[g_{j-1/2}^{n-1/2}K_n^{-1}(g_{j-1/2}^n - g_{j-1/2}^{n-1}) - w_{j-1/2}^{n-1/2}K_n^{-1}(f_{j-1/2}^n - f_{j-1/2}^{n-1})] \end{aligned} \tag{22}$$

$$\begin{aligned} h_j^{-1}[(et)_j^{n-1/2} - (et)_{j-1}^{n-1/2}] + h_j^{-1}[(dgw)_j^{n-1/2} - (dgw)_{j-1}^{n-1/2}] &= -(P_1)_{n-1/2}(ft)_{j-1/2}^{n-1/2} + \xi_{n-1/2} \\ &\quad \times [g_{j-1/2}^{n-1/2}K_n^{-1}(s_{j-1/2}^n - s_{j-1/2}^{n-1}) - t_{j-1/2}^{n-1/2}K_n^{-1}(f_{j-1/2}^n - f_{j-1/2}^{n-1})] \end{aligned} \tag{23}$$

In the formulas

$$\xi_{n-1/2} = \xi_n - \frac{K_n}{2}, \quad (P_1)_{n-1/2} = P_1(\xi_{n-1/2})$$

$$(g^2)_{j-1/2}^{n-1/2} = [(g^2)_j^n + (g^2)_j^{n-1} + (g^2)_{j-1}^n + (g^2)_{j-1}^{n-1}]/4$$

$$(bw)_j^{n-1/2} = [(bw)_j^n + (bw)_j^{n-1}]/2$$

$$(et)' = h_j^{-1}[(et)_j^{n-1/2} - (et)_{j-1}^{n-1/2}]$$

$$\left(\frac{\partial s}{\partial \xi}\right)_{j-1/2}^{n-1/2} = K_n^{-1}(s_{j-1/2}^n - s_{j-1/2}^{n-1})$$

The remainder are analogously deduced.

The boundary conditions are:

$$f_0^n = 0,\ g_0^n = 0,\ g_J^n = 1 \qquad (24)$$

(1)

$$s_0^n = s_w \text{ 或 } t_0^n = t_w,\ s_J^n = 1$$

Key: (1) Or.

C. Numerical Solution

If we calculate beginning from the $\xi = \xi_{n-1}$ station, then f_j^{n-1}, g_j^{n-1}, w_j^{n-1}, s_j^{n-1} and t_j^{n-1} are known ($0 \leqslant j \leqslant J$) and it is necessary that the f_j^n, g_j^n, w_j^n, s_j^n and t_j^n values in the ξn station area be a total of (5J+5) and equations (19)-(24) form a set of equations of these (5J+5) unknown quantities. In order to simplify calculations, we broke them up into two sets. We used the corresponding boundary conditions in the first set of equations (19), (20) and (22) as well as (24) to first solve the (3J+3) unknown quantities f_j^n, g_j^n and w_j^n; afterwards, we used the remaining boundary conditions in the second set of equations (21), (23) as well as (24) to solve the (2J+2) unknown values s_j^n, and t_j^n and then used the new s_j^n and t_j^n values to replace the coefficient values of the first set of equations and again solve the new f_j^n, g_j^n and w_j^n values. It is repeated in this way until we satisfy certain convergence conditions.

For the first set of equations, we first separate and classify the function values of the ξ_n and ξ_{n-1} stations in formula (22) into equal formulas on the left and right sides and afterwards use the Newtonian normal line to change this set of equations, that is:

We introduce iteration of $\left\{ f_j^{(i)},\ g_j^{(i)},\ w_j^{(i)} \right\}$ i=0,1,2....

The initial value is

$$
\begin{aligned}
&f_0^{(0)} = 0\,,\ g_0^{(0)} = 0\,,\ w_0^{(0)} = w_0^{n-1}\\
&f_j^{(0)} = f_j^{n-1},\ g_j^{(0)} = g_j^{n-1},\ w_j^{(0)} = w_j^{n-1}\ (1 < j < J-1)\\
&f_J^{(0)} = f_J^{n-1},\ g_J^{(0)} = 1\,,\ w_J^{(0)} = w_J^{n-1}
\end{aligned}
$$

For high order iteration we let

$$
\begin{aligned}
f_j^{(i+1)} &= f_j^{(i)} + \delta f_j^{(i)}\\
g_j^{(i+1)} &= g_j^{(i)} + \delta g_j^{(i)}\\
w_j^{(i+1)} &= w_j^{(i)} + \delta w_j^{(i)}
\end{aligned}
$$

Substituting in the first set of equations and omitting the second order terms of δ f, δ g and δ w, we then obtain the set of linear equations (for convenience of calculations, we omit the right upper corner (i) of each term):

$$\delta f_j - \delta f_{j-1} - \frac{h_j}{2}(\delta g_j + \delta g_{j-1}) = \Upsilon 1_j \tag{25}$$

$$\delta g_j - \delta g_{j-1} - \frac{h_j}{2}(\delta w_j + \delta w_{j-1}) = \Upsilon 3_j \tag{26}$$

$$(s1)_j \delta w_j + (s2)_j \delta w_{j-1} + (s3)_j \delta f_j + (s4)_j \delta f_{j-1} + (s5)_j \delta g_j + (s6)_j \delta g_{j-1} = \Upsilon 2_j \tag{27}$$

In the formulas

$$
\begin{aligned}
&\Upsilon 1_j = f_{j-1}^{(i)} - f_j^{(i)} + h_j g_{j-1/2}^{(i)}\\
&\Upsilon 3_j = g_{j-1}^{(i)} - g_j^{(i)} + h_j w_{j-1/2}^{(i)}\\
&\Upsilon 2_j = R1_{j-1/2}^{n-1} - [h_j^{-1}(b_j^{(i)} w_j^{(i)} - b_{j-1}^{(i)} w_{j-1}^{(i)}) + ((P_1)_n + \alpha_n)(fw)_{j-1/2}^{(i)}\\
&\qquad + ((P_2)_n + \alpha_n)(g^2)_{j-1/2}^{(i)} + \alpha_n (w_{j-1/2}^{n-1} f_{j-1/2}^{(i)} - f_{j-1/2}^{n-1} w_{j-1/2}^{(i)})]
\end{aligned}
$$

$$
\begin{aligned}
(s1)_j &= h_j^{-1} b_j^{(i)} + \frac{1}{2}[((P_1)_n + \alpha_n) f_j^{(i)} - \alpha_n f_{j-1/2}^{n-1}]\\
(s2)_j &= -h_j^{-1} b_{j-1}^{(i)} + \frac{1}{2}[((P_1)_n + \alpha_n) f_{j-1}^{(i)} - \alpha_n f_{j-1/2}^{n-1}]\\
(s3)_j &= \frac{1}{2}[((P_1)_n + \alpha_n) w_j^{(i)} + \alpha_n w_{j-1/2}^{n-1}]\\
(s4)_j &= \frac{1}{2}[((P_1)_n + \alpha_n) w_{j-1}^{(i)} + \alpha_n w_{j-1/2}^{n-1}]\\
(s5)_j &= -[(P_2)_n + \alpha_n] g_j^{(i)}\\
(s6)_j &= -[(P_2)_n + \alpha_n] g_{j-1}^{(i)}
\end{aligned}
$$

$$
\begin{aligned}
R1_{j-1/2}^{n-1} = &-h_j^{-1}[(bw)_j^{n-1} - (bw)_{j-1}^{n-1}] + [-(P_1)_n + \alpha_n](fw)_{j-1/2}^{n-1} - [-(P_2)_n\\
&+ \alpha_n](g^2)_{j-1/2}^{n-1} - (P_2)_n(\rho_e/\bar{\rho})_{j-1/2}^{n} - (P_2)_{n-1}(\rho_e/\bar{\rho})_{j-1/2}^{n-1}
\end{aligned}
$$

$$\alpha_n = \xi_{n-1/2}/(\xi_n - \xi_{n-1}) = K_n^{-1}\xi_{n-1/2}$$

In the calculations, the first time we substitute the flow parameters in the $\xi = \xi_{n-1}$ station area into $(\varepsilon_m)_i$ and (ε'_m). b is found from the formula and we let $(\varepsilon_m)_i = (\varepsilon'_m)$. We find the y_c value of the intersecting area of the inner and outer layers of the boundary layer. The boundary conditions remain unchanged in the iterations, that is, we take

$$\delta f_0^{(i)} = 0,\ \delta g_0^{(i)} = 0,\ \delta g_j^{(i)} = 0,\ i = 0,\ 1,\ 2,\ \cdots\cdots$$

The set of equations (25), (26) and (27) form a block of three diagonal matrices and by using matrix algebra we can solve the perturbation quatities ($\delta f_j^{(i)}$, $\delta g_j^{(i)}$ and $\delta w_j^{(i)}$). We add them to the above one time iteration value until calculation convergence and the convergence data takes $|\delta w_w| < \varepsilon$. The lower symbol w indicates the wall surface value and ε is the assigned small quantity.

This paper calculates beginning from $\xi = 0$, the right side of formula (16) is zero, the flow is assumed to be a laminar flow ($\varepsilon_m = 0$) and we can suppose an iteration solution of the initial velocity distribution and enthalpy distribution (or temperature distribution); the next step calculates the parameters of each ξ station based on the turbulent flow ($\varepsilon_m \neq 0$).

After finding a preliminary solution of the set of momentum equations, we can solve the energy equation and following the above procedure classify each function value of the ξ_n and ξ_{n-1} stations in the set of equations in (23) to the two sides of the formula being equal and write the set of linear equations as

$$(s11)_j t_j + (s12)_j t_{j-1} + (s13) s_j + (s14)_j s_{j-1} = (R12)_j \tag{28}$$

In the formula

$$(s11)_j = h_j^{-1} e_j^n + \frac{1}{2}((P_1)_n + \alpha_n) f_{j-1/2}^n - \frac{1}{2}\alpha_n f_{j-1/2}^{n-1}$$

$$(s12)_j = -h_j^{-1} e_{j-1}^n + \frac{1}{2}((P_1)_n + \alpha_n) f_{j-1/2}^n - \frac{1}{2}\alpha_n f_{j-1/2}^{n-1}$$

$$(s13)_j = -\alpha_n g_{j-1/2}^{n-1/2}$$

$$(s14)_j = -\alpha_n g_{j-1/2}^{n-1/2}$$

$$(R12)_j = -h_j^{-1}[(et)_j^{n-1} - (et)_{j-1}^{n-1}] - 2h_j^{-1}[(dgw)_j^{n-1/2} - (dgw)_{j-1}^{n-1/2}]$$
$$-(P_1)_{n-1}(ft)_{j-1/2}^{n-1} - 2\alpha_n g_{j-1/2}^{n-1/2} s_{j-1/2}^{n-1} + \alpha_n s_{j-1/2}^{n-1}(f_{j-1/2}^{n-1} - f_{j-1/2}^n)$$

When the ξ_{n-1} station momentum equation, energy equation as well as ξ_n station momentum equation solutions are known, the above coefficients $(s12)_j$ etc. can be found and equations (21) and (28) and the corresponding boundary conditions form a block of three diagonal matrices and we find s_j^n and t_j^n. This paper calculates beginning from the $\xi=0$ area, this area's $a_n=0$ and thus equation (28) is simplified into:

$$(s11)_j t_j + (s12)_j t_{j-1} = (R12)_j \tag{29}$$

In $(s11)_j$ and $(s12)_j$, we also omit the terms containing a_n. At this time, under adiabatic wall or given $t=t_w$, the first block element is singular and thus the block element must carry out different processing and arrangement (see Reference [12]).

III. Shock Wave and Boundary Layer Disturbance Corrections

As mentioned previously, when there is transonic flow over a compression corner, the inverse pressure gradient along the flow direction caused by the shock waves formed in the area of the compression corner causes the boundary layer in front of the angular point to become thick which changes the effective form of the physical surface and thus changes the pressure distribution along the periphery of the boundary layer. It conversely also influences the development of the boundary layer and it repeats thusly until establishing an equilibrium. In this way, for still unseparated flows, we first calculate the inviscid pressure distribution over a compression corner and based on this solve the boundary layer equation and determine displacement thickness δ^* as well as its changing rate $\frac{d\delta^*}{dx}$ which changes with x. This changing rate is the approximate value of the streamline diflection angle induced from the thickening of the boundary layer. This is also the ratio of the induced normal velocity and velocity u_c on the periphery and it is written as:

$$\frac{v}{u_e} \approx \theta_d \approx \frac{d\delta^*}{dx}$$

If the included angle of the original physical surface's form and the distant front overtaking flow is θs, then the included angle of the physical surface's effective form and distant overtaking flow after viscous disturbance is

$$\theta_T = \theta_s + \frac{d\delta^*}{dx} \qquad (30)$$

Having θ_T, by using the Van Dyke unified supersonic-hypersonic small disturbance theory [14], we can find the new pressure distribution

$$\frac{p_e}{\gamma M_\infty^2 p_\infty} = \frac{1}{\gamma M_\infty^2} + \theta_T^2\left(\frac{\gamma+1}{4} + \sqrt{\left(\frac{\gamma+1}{4}\right)^2 + \frac{1}{(M_\infty^2-1)\theta_T^2}}\right) \qquad (31)$$

Pressure gradient parameter P_2 is

$$P_2 = \frac{x}{u_e}\,\frac{du_e}{dx} = -\frac{x}{\rho_e u_e^2}\,\frac{dp_e}{d\theta_T}\,\frac{d\theta_T}{dx} \qquad (32)$$

The other parameters on the periphery of the boundary layer are all found with p_c based on the isentropic relationship.

IV. Calculations and Results

This paper carried out calculations with $M_\infty = 2.85$, $T_0 = 268K$, $Re_\infty / L = 6.7 \times 10^7$/meters, adiabatic wall surface and compression corner a=16°. The x direction uses 25 grid points and the η direction grid points number 37 from the $\xi = 0$ area to 52 grid points in the final ξ station area. For the estimation of turbulent flow boundary layer thickness $\eta_\infty(\xi)$ which enlarges with ξ used here see Reference [12]. The ξ direction grids are equidistant and $\Delta\xi = 0.04$; the η direction grid is the closest distance from the wall, $\Delta\eta_1 = h_1 = 0.01$, m=1.14, $\Delta\eta_2 = h_2$ etc. are calculated according to the above formula $h_j = mh_{j-1}$. The angular point is located in the x=0.5 area, that is, between Nx=13 and Nx=14, and Nx is the number of the x direction station location. The $\frac{1}{\rho_c \mu_c}$ of the $\frac{1}{\rho_c \mu_c} \frac{d}{dx} (\rho_c \mu_c)$ term in P_1 uses the mean value of the two front and back angular points; when we consider the existence of the boundary layer, use of the pressure strength rise of the shock waves is not sudden but is completed in any multiple distance along the wall surface equal to the thickness of the local boundary layer. For this reason, when beginning calculations, we complete the levelling of the angular point's front and back pressure rise in the four x direction grids. In order to simplify the amount of calculations, when $\xi > 0$, we use the relational formula of the enthalpy and velocity distribution when $P_r \neq 1$

$$\frac{\bar{H}}{H_e} = a + b \frac{\bar{u}}{u_e} + c \left(\frac{\bar{u}}{u_e} \right)^2$$

Substituting the calculation of the energy equation, coefficients a,b and c are determined by the adiabatic wall's boundary conditions. Calculations on the 20,000 times/second FacoM 230 computer only requires three times of iteration to be able to obtain relatively good results. The C.P.U. calculation time without carrying out iteration is 33 seconds while the C.P.U. calculation time with carrying out iteration is one minute and 20 seconds. The appended figures draw the wall surface pressure distribution, friction damping distribution as well as the velocity distribution of a station location and they accord well with the wall surface pressure distributions of Reference [15].

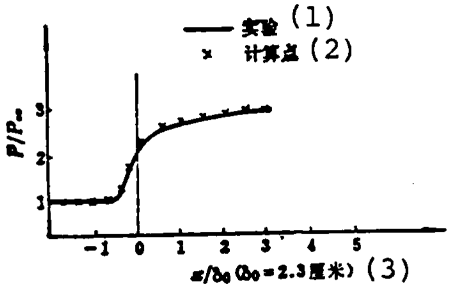

Fig. 1 Comparison (with Reference [15]) of surface pressure distribution.

Key: (1) Test; (2) Calculation point; (3) Centimeters.

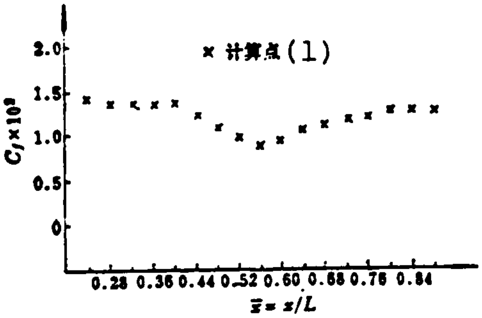

Fig. 2 C_f distribution along compression surface (the angular point is in the $\bar{X}$=0.50 area, L=13.8cm).

Key: (1) Test point.

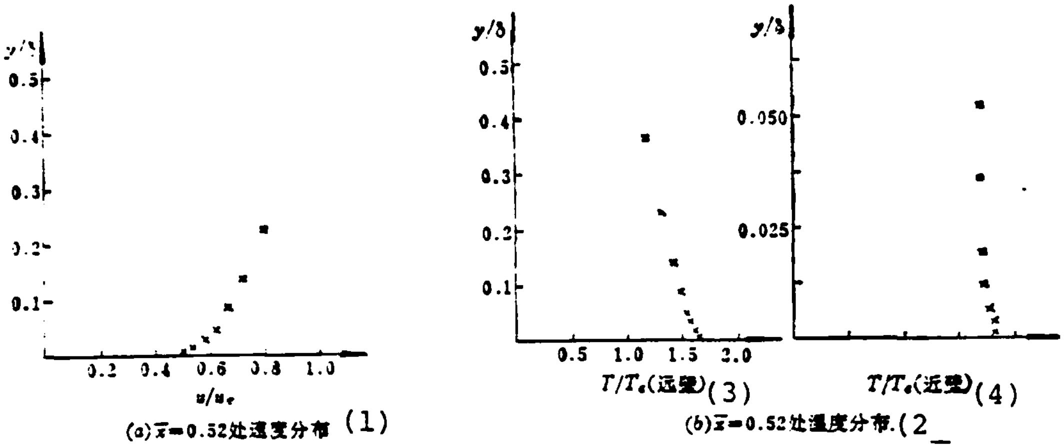

(a) velocity profile
at $\bar{x}=0.52$

(b) temperature profile
at $\bar{x}=0.52$

Fig. 3

Key: (1) $\bar{x}$=0.52 area velocity distribution; (2) $\bar{x}$=0.52 area temperature distribution; (3) Distant wall; (4) Near wall.

References

[1] G. Drougge: Experimental investigation of the influence of strong adverse pressure gradients on turbulent boundary layers at supersonic speeds. Paper presented at the 8th International Congress on Theoretical and Applied Mechanics, 1952.

[2] H.W. Liepmann, A. Roshko and S. Dhawan: On reflection of shock waves from boundary layers, N.A.C.A. report 1100.

[3] D.H. Holder and G.E. Gadd: The interaction between shock waves and boundary layers and its relation to base pressure in supersonic flow. Paper No. 8, Symposium on Boundary Layer Effects in Aerodynamics, 1955.

[4] D.R. Chapman, D.M. Kuehn and H.K. Larson: Investigation of separated flows in supersonic and subsonic streams with emphasis on the effect of transition, N.A.C.A.T.N3869, 1957.

[5] B.L. Reeves: Results of a strong interation wake like model of supersonic separated and reattaching turbulent flows. AIAA.J. April, 1971.

[6] V. Zakkay: Two dimensional turbulent boundary layer separation on a flat plate with ramp at free stream Mach numbers of 3.7 and 6.3 in supersonic and hypersonic flow. ADAO 14729.

[7] M.J. Werle and S.D. Bertke: Application of an interacting boundary layer model to the supersonic turbulent separation problem. ADAO 29328.

[8] R. Ariele and J.D. Murphy: Pseudo-direct solutions to the boundary layer equations for separated flow. AIAA paper 79-0139.

[9] J.S. Shang and W.L. Hankey: Numerical solution of Navier-Stokes equation for supersonic turbulent flow over a compression ramp. AIAA paper 75-3.

[10] Zhang Hanxin, Lu Linsheng, Yu Zechu and Ma Zhankui, Explicit and implicit difference solutions of supersonic and hypersonic viscous gas separation flows. Journal of Aerodynamics, No. 3, 1980.

[11] Jiang Dachun, Use of the implicit-explicit method to solve the separation flows of supersonic turbulent flows flowing passed compression corners, Journal of Aerodynamics, No. 3, 1982.

[12] T. Cebeci, P. Bradshaw and J.H. Whitelaw: "Engineering calculation method for turbulent flow" N78-20091.

[13] Cao Qipeng, Certain problems concerning the turbulent flow boundary layer difference solution. Journal of Nanjing Aeronautics Institute, No. 1, 1979.

[14] M.D. Van Dyke: A study of hypersonic small-disturbence theory. NACA TN 3173, 1954.

[15] S.M. Bogdonoff et al, A detailed study of attached and separated compression corner flow fields in high Reynolds number supersonic flow. AIAA paper 78-1167.

OPTIMUM DESIGN OF AN AIRCRAFT WING STRUCTURE WITH MULTIPLE CONSTRAINTS BY THE DIRECT-VISION CRITERIA METHOD

Penned by Li Linang
Shenyang Aircraft Corporation

Abstract

This paper introduces an optimized computer program SAFDOP which uses the direct-vision criteria method for a wing surface structure with multiple constraints. This program can separately carry out analysis, optimization and synthetic optimization calculations of stress, displacement, flutter and static aeroelasticity. We used the alternate constraint method for synthetic optimization calculations. Aside from the stress constraints using the full stress method, each of the other constraints used the uniform derivative criteria. For practical purposes, we used the element linking weight as an independent design variable, in the optimum design the automatic sieve selection design variable and other methods were used and we also considered the automatic generation of initial numerical data. We used this program to calculate a typical fighter wing and it proved to be feasible.

I. Introduction

In order to raise the maneuverablity of fighters, it is necessary to use a thin wing with medium aspect ratio and medium sweepback angle. The structural design of this type of wing must at the same time consider the strength, flutter, static aeroelasticity and displacement etc. requirements; and to raise the thrust-weight ratio of the aircraft, it is also necessary when satisfying these conditions to cause the designed structural weight to be minimum. References [1,2,5] also only consider optimization calculations under one type of constraint condition. References [3,4] only performs optimization calculations under two types of constraint conditions. The focus of this paper is to resolve and simultaneously satisfy the optimization calculations of wing surface structures with various types of constraint conditions. In this way, we can reduce the numerical data transfer errors, save on computer time, shorten the design period and reach the goal of the structure's minimum weight design.

II. Numerical Data Generation

In order to reduce the copying and transmission work of initial numerical data, the SAFDOP system considers the automatic generation of intial numerical data and information. Its contents include: (1) model node point automatic numbering; (2) generation of nodal point coordinates; (3) generation of element information included in element linking; (4) the interchange of information between the element chain and element; (5) generation of the quality, materials, structural parameters and the permitted stress etc. information.

III. Analysis of the Structure

1. Analysis of Stress

The analysis of stress uses the finite element displacement method and the displacement vector is obtained by the following formula which uses the variable band width elimination method.

$$\{P\}=[K]\{\delta\} \qquad (1)$$

With the displacement of the element, we find the element's inner force based on the following formula

$$\{S\}=[k]\{\delta\} \qquad (2)$$

We then find the stress of the element based on the relationship of the inner force and stress. Within this, $\{P\}$ is the load array; [K] is the structure's total stiffness matrix; [k] is the structural element's stiffness matrix; $\{S\}$ is the structure's inner force array; and $\{\delta\}$ is the structure's displacement array.

2. Analysis of Flutter

The analysis of flutter uses the following equation

$$-\omega^2 \sum_{R=1}^{N} M_{nR} q_R + \omega_n^2 (1 + i g_n) M_{nn} q_n = K \omega^2 \sum_{R=1}^{N} a_{nR} q_R \qquad (3)$$

$$K = 2\pi (b_0 / k)^2 \rho$$

In the formula, ω is the flutter frequency; q is the generalized coordinate; b_o is the half root chord length; g is the structure's damping coefficient; N is the number of the degrees of freedom; ω_n is the natural vibraton frequency; a_{nR} is the generalized aerodynamic force; M_{nR} is the generalized mass; k is the reduced frequency ($k=\frac{b_o \omega}{v}$, v is the flutter velocity), footnote n, R=1,2,....., N.

The sturucture's intrinsic frequency ω and form f are calculated according to the following formula which uses the iteration method

$$\{f\} = -\omega^2 [C^{YY}] \left[\diagdown M \diagdown\right] \{f\} \qquad (4)$$

In the formula, $[C^{YY}]$ is the flexibility matrix and $\left[\diagdown M \diagdown\right]$ is the mass matrix.

$[C^{YY}]$ is obtained from formula [1] and we use the curved surface spline function to interpose to each mass point; after obtaining the intrinsin form, we use the curved surface spline function to interpose on 12 air flow direction tangent planes (each tangent plane uses 4 points), then we use the cubic curve to fit the form of each air flow direction tangent plane and provide non-constant aerodynamic force for calculations; the non-constant aerodynamic force is calculated by the subsonic kernel function method and it allows the use of 9 control points; we use the v-g method to solve the flutter equation.

3. Analysis of Static Aeroelasticity

Analysis of aeroelasticity uses the following equation

$$\{\alpha_f\} = \{\alpha_0\} + \frac{1}{2}\rho v^2[C^{\theta Y}][A]\{\alpha_f\} \qquad (5)$$

In the formula, a_o is the distribution of the initial attack angle; a_f is the final attack angle distribution after considering the aeroelastic effects; $[C^{\Theta Y}]$ is the corner flexibility matrix; [A] is the aerodynamic force effect coefficient matrix.

Aerodynamic force effect coefficient matrix [A] is calculated by the Woodward method and we use the curved surface spline function to interpose the C^{YY} of the structure's nodal point area to each aerodynamic force's divided characteristic point and then find the air flow direction's slope and obtain $C^{\Theta Y}$.

For problems corresponding to different static aeroelasticity, we give a_o and after solving a_f based on requirements we find the force or moment of force and lastly find ratio K of the force or moment of force considering the aeroelasticity effects and the rigid body value.

IV. The Structure's Optimum Design

1. Design Variables

In order to avoid the changes of the structure's element dimensions after optimization not satisfying technical requirements and at the same time to reduce the number of design variables so as to make optimization calculations in medium and small computers convenient, the SAFDOP uses the element linking weight as the design variable.

The element linking is defined as the joining of any interconnected similar type elements. One element linking includes any similar type elements and the dimensions of these elements are obtained from two control dimension linear interpolations of the element linking.

2. Optimum Design of Stress Constraints

We use the full stress method for stress constraint optimization. Under given structural layout and materials conditions as well as many types of load effects, each element at the least has the operating stress reach an allowable value under a type of load effect or reach limiting dimensions. The expression of its constraint conditions is:

$$g_1=\left|1-\frac{\sigma_{i\max}}{(\sigma_i)}\right|\leqslant\varepsilon \qquad (6)$$

(1)

$$g_2=1-\frac{x_{i\min}}{x_i}\geqslant 0 \quad \text{或} \quad \frac{x_{i\max}}{x_i}-1\geqslant 0 \qquad (7)$$

Key: (1) Or.

In the formulas, $\sigma_{i\max}$ is the maximum operating stress of the i number elements under many types of load effects; (σ_i) is the permissable stress of the i number elements, its positive and negative signs are determined by the positive and negative signs of $\sigma_{i\max}$, it can be a constant value and it can also be the buckling damage stress which changes with the design variables in the iteration process; ε is the permissable error and is predetermined by the designer; x_i, $x_{i\max}$ and $x_{i\min}$ are separately the element's calculated dimensions and maximum and minimum dimensions corresponding to the i number design variables. In order to attain the above goals, it is necessary to carry out iteration. The iteration formula is

$$W_i^{K+1}=\left(\frac{\sigma_{i\,\max}^{K}}{(\sigma_i)^{K}}\right)^{R} W_i^{K} \qquad (8)$$

In the formula, W_i is the weight of the i number elements (or element linking), K indicates the number of iterations, R is the superrelaxation coefficient. It is used to regulate the correction quantity, it has a relatively large effect on the convergence speed and it is mainly determined by the structure's form and constraint conditions.

The definition of the element linking's full stress is that in each element linking, at least two points of stress not on the same tangent plane reach the constraint condition requirements of full stress and each of the other points do not allow excessive stress.

3. Single Constraint Optimization Calculations of the Displacement, Flutter and Static Aeroelasticity

Single constraint optimization of displacement, flutter and static aeroelasticity all use uniform derivative criteria. We take the design variable to be W, the structural weight of the wing surface is objective function F, g is the constraint function and then the Lagrangian function is

$$\Phi(W)=F(W)+\lambda g(W) \qquad (9)$$

The limiting value condition is

$$\frac{\partial\Phi(W)}{\partial W_i}=\frac{\partial F(W)}{\partial W_i}+\lambda\frac{\partial g(W)}{\partial W_i}=0$$

As a result

$$\frac{\partial g(W)}{\partial W_i}=-\frac{\partial F(W)}{\partial W_i}\Big/\lambda$$

and because

$$\frac{\partial F(W')}{\partial W'_i}=1$$

therefore

$$\frac{\partial g(W')}{\partial W'_i}=-\frac{1}{\lambda}=\text{常数}\ (1) \qquad (10)$$

Key: (1) Constant.

We can know from the above formulas that for situations with single constraints, when the weight partial derivatives of the constraint function for each element (or element linking) are all constants, the structural weight reaches minimum value.

Its constraint expressions are separately:

For displacement constraints

$$g_1=\left|1-\frac{\delta}{(\delta)}\right|\leqslant\varepsilon \qquad (11)$$

$$g_2=1-\frac{x_{i\,\min}}{x_i}\geqslant 0 \quad \overset{(1)}{\text{或}} \quad \frac{x_{i\,\max}}{x_i}-1\geqslant 0 \qquad (12)$$

Key: (1) Or.

In the formulas, δ is the generalized displacement under aerodynamic load effects. It can be the torsional angle or bending angle of a certain tangent plane on the wing or the deflection of a certain nodal point or the turning angle of a certain spar; (δ) is its corresponding permissable value. These displacement constraints can be on nodal points as well as not on nodal points. The displacement not on nodal points is obtained based on the linear interpolation of the two adjacent nodal point displacements; x_{imax} and x_{imin} are separately the element's maximum and minimum limiting dimensions corresponding to the i number design variables.

For the flutter constraints

$$g_1 = \left|1 - \frac{v_f}{(v_f)}\right| \leqslant \varepsilon \tag{13}$$

$$g_2 = 1 - \frac{x_{i\,\min}}{x_i} \geqslant 0 \quad \overset{(1)}{\text{或}} \quad \frac{x_{i\,\max}}{x_i} - 1 \geqslant 0 \tag{14}$$

Key: (1) Or.

In the formulas, v_f is the claculated flutter speed; (v_f) is the flutter speed needed to be reached.

For the static aeroelastic constraints

$$g_1 = \left|1 - \frac{K}{(K)}\right| \leqslant \varepsilon \tag{15}$$

$$g_2 = 1 - \frac{x_{i\,\min}}{x_i} \geqslant 0 \quad \overset{(1)}{\text{或}} \quad \frac{x_{i\,\max}}{x_i} - 1 \geqslant 0 \tag{16}$$

Key: (1) Or.

In the formulas, K is the ratio of the calculated flexible wing surface force (moment of force) and the stiff wing surface value; (K) is the K value which needs to be reached.

When separately satisfying these constraint conditions, in order to reach the goal of uniform derivatives needed for carrying out iteration, the iteration formulas is similar to iteration formula (8) for full stress design, that is

$$W_i^{K+1} = \left(\frac{(\partial g/\partial W_i)^K}{(\partial g/\partial W)^K_{\underset{(1)}{}}}\right)^{\eta} W_i^K \tag{17}$$

Key: (1) Objective.

In the formula, $(\partial g/\partial W)_{\text{objective}}$ is called the objective derivative and it has the same value for all of the design variables. In reality, it controls the parameters of the design variable's changing step length and based on each step we anticipate obtaining constraint function increment Δg and determine the objective derivative values.

For the displacement constraints

$$\Delta g=\sum_{i=1}^{n}\frac{1}{2}\left[\left(\frac{\partial g}{\partial W_i}\right)^{K}+\left(\frac{\partial g}{\partial W}\right)^{K}_{\underset{(1)}{\text{目标}}}\right](W_i^{K+1}-W_i^{K}) \tag{18}$$

Key: (1) Objective.

For the flutter and static aeroelastic constraints

$$\Delta g=\sum_{i=1}^{n}\left(\frac{\partial g}{\partial W_i}\right)(W_i^{K+1}-W_i^{K}) \tag{19}$$

In order to control the step length, we take $\Delta g=\frac{(g)-g}{n}$, n is the positive integer given by the designer, R always takes 1/2 for the flutter and displacement constraints and 1 for the static aeroelastic constraints.

For the flutter and static aeroelastic constraints.

The calculation expression of the objective derivative is jointly obtained from formulas (17) and (19):

$$\left(\frac{\partial g}{\partial W}\right)^{K}_{\underset{(1)}{\text{目标}}}=\sqrt[R]{\frac{\sum_{i=1}^{n}\left(\frac{\partial g}{\partial W_i}\right)_{K}^{K+1}W_i^{K}}{(\Delta g)+\sum_{i=1}^{n}\left(\frac{\partial g}{\partial W_i}\right)^{K}W_i^{K}}} \tag{20}$$

Key: (1) Objective.

In the formula, n is the number of design variables.

For the displacement constraints, we can obtain the corresponding objective derivative expression in the same way from formulas (17) and (18).

In fact, when we only have the main effect of the elements on the constraint function, the constraint function can gradually become uniform in the iteration process for its derivative. These elements are called "critical elements". However, when the constraint effects are not great or have an inverse effect (i.e. when the element has a negative derivative and there is an increase in the structural weight, the constraint function value is actually reduced) or for elements wherein the constraints have major effects and the dimensions exceed the maximum limiting value, there derivatives will tend to be not uniform. The dimensions of these elements are determined by the limiting geometric dimensions and these elements are called "non-critical elements".

In order to quicken convergence, when saving on computer time, during iteration, we use the automatic sieve selection design variable method which is the automatic elimination during each iteration cycle of design variables which belong to negative derivatives or have already reached the smallest dimensions and the derivative is smaller than the objective derivative.

4. Calculation of Synthetic Optimization

(1) Constraint Conditions

$$g_1 = \left| 1 - \frac{\sigma_{i\,\max}}{(\sigma)} \right| \geqslant 0 \tag{21}$$

$$g_2 = 1 - \frac{\delta}{(\delta)} \geqslant 0 \tag{22}$$

$$g_3 = \frac{v_f}{(v_f)} - 1 \geqslant 0. \tag{23}$$

$$g_4 = \frac{K}{(K)} - 1 \geqslant 0 \tag{24}$$

$$g_5 = 1 - \frac{x_{i\,\min}}{x_i} \geqslant 0 \tag{25}$$

$$g_6 = \frac{x_{i\,\max}}{x_i} - 1 \geqslant 0 \tag{26}$$

(2) Optimization Method

The optimization calculation when the wing surface's structure simultaneously satisfies the requirements of the above two types or more constraints (aside from the limiting geometric constraints), it is called synthetic optimization calculations or multiple constraints' optimization calculations. The synthetic optimization method uses the constraint rotational method which transforms the multiple constraint problem into the processing of a series of single constraints. We then use the selection of the major constraint to reach the goal of reducing the number of constraints. The specific method is on the basis of the full stress design, we check whether or not the constraints are satisfied and if they are this is the state of synthetic optimum design. If they are not satisfied, then we distinguish by means of the major constraints, select the most "dangerous" constraints and optimize them. Afterwards, we check whether or not the remaining constraints are satisfied and if they are we transfer into the full stress calculation, otherwise we carry out major constraint selection and repeat the above process until the constraint conditions are all satisfied and continue until the difference of the weights calculated from the full stress of the two cycles reaches the predicted value. That is, the structure reaches the state of synthetic optimum design. At this time, the elements in the structure are divided into different types of "critical elements". For example, the "stress critical elements", "displacement critical elements", "flutter critical elements", "aileron critical elements" and minimum or maximum geometric dimension elements". All of these elements separately attain the requirements of each optimization criterion. That is, the "stress critical elements" attain the requirements of full stress calculations and the "displacement", "flutter" and "aileron efficiency" critical elements all satisfy the requirements of uniform derivative criteria. Naturally, when the wing surface structure is in a synthetic optimum state, these "critical elements" do not necessarily exist simultaneously but the number of critical elements which appear is related to the constraint characteristics. However, it is necessary to point out that when we enter in certain constraint optimization, the "critical elements" controlled by other constraints can only increase the dimensions and only the dimensions of its own "critical element" can change up and down; the "critical elements" can be transformed during the optimization process. For example, when the "stress critical element" enters into flutter constraint optimization, this increases the dimensions and changes it into a "flutter critical element". See Fig. 1 for a flow chart of synthetic optimization.

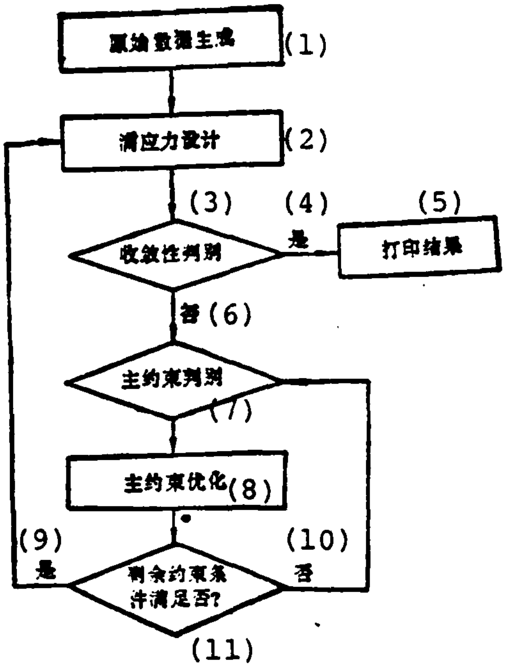

Fig. 1 Flow chart of synthetic optimization.

Key: (1) Original data generation; (2) Full stress design; (3) Convergence discrimination; (4) Is; (5) Printed results; (6) Is not; (7) Main constraint discrimination; (8) Main constraint optimization; (9) Is; (10) Is not; (11) Are the remaining constraint conditions satisfied or not?

V. Examples of Utilization

We will here only give one example to show the use of this program to calculate many types of wing surface structures. The calculation model is as shown in Fig. 2. For thin wings with medium aspect ratios and medium sweepback angles, the root and fuselage linking uses four fixed points and one hinge point and the form is a multiwall structure. Aside from the three bent beam roots being steel pieces, the other materials are all aluminum alloy. We used the variable section isometric force bar element and quadrilateral cut plate element to simulate the spar, rib flange and skin; we used a symmmetric cut trapezoidal plate element to simulate the spar and composite plate of the ribs; we used an equal section bar element to simulate the elastic fixed connecting of the wing and fuselage; we used the "fictitious bar" with relatively large stiffness to simulate the front and rear end structures. We used symmetrical conditions and the half structure for calculations. The calculation model had a total of 106 nodal points and 318 degrees of freedom; in the flutter calculations, we used 300 mass points and in the aileron efficiency calculations there were 44 aerodynamic blocks.

We separately carried out optimization calculations of the element linking's full stress flutter, aileron efficiency, wingtip turning angle and their synthesis. The wing structure's weight is given that the element linking's full stress state was 451 kilograms, the flutter speed was 485 meters/second, the aileron efficiency was 0.088 and the wingtip turning angle was a 0.0033 radian. The design required that the flutter speed be 550 meters/second, the aileron efficiency K value be 0.3 and the wingtip turning angle be 0.03. The calculation results are given in Figs. 4-7.

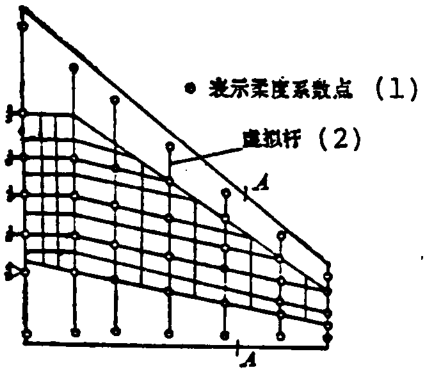

Fig. 2 Model of wing structure.

Key: (1) Shows the flexibility coefficient point; (2) Fictitious bar.

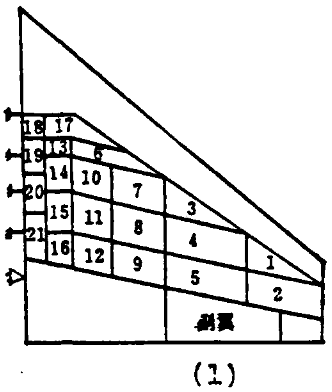

Fig. 3 Typical model of skin element linking.
Key: (1) Aileron.

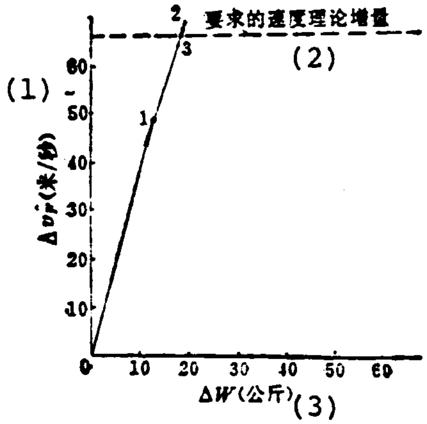

Fig. 4 Iterative process of flutter constraints.
Key: (1) Meters/second; (2) Required velocity theoretical increment; (3) Kilograms.

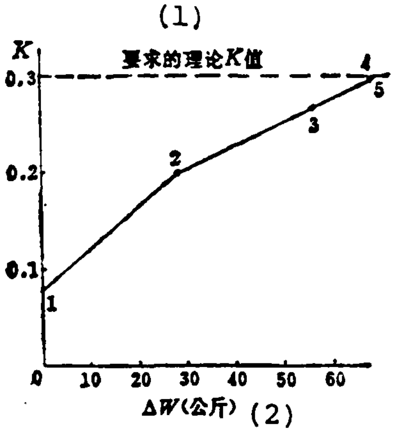

Fig. 5 Iterative process of aileron efficiency constraints.
Key: (1) Required theoretical K value; (2) Kilograms.

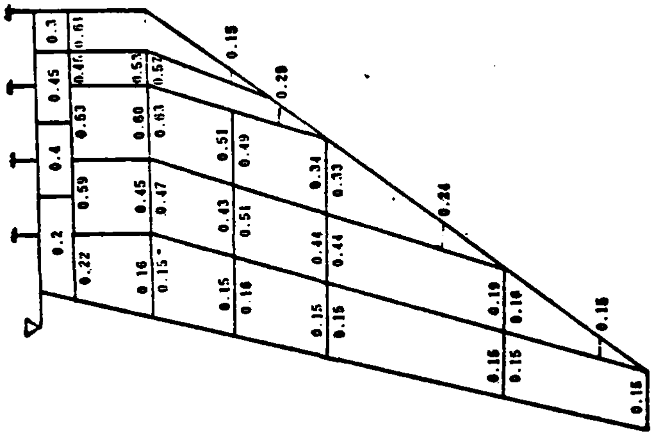

Fig. 6 Distribution of skin thickness for full stress design.

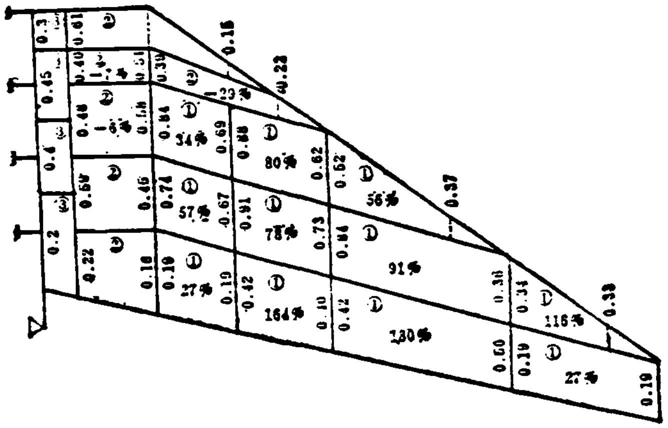

Fig. 7 Distribution of skin thickness for synthetic optimum state.

In the figure: % is the thickness increment of the critical element of the skin thickness relative full stress design; ① is the aileron efficiency critical element; ② is the stress critical element; ③ is the minimum dimension element.

The simple constraint calculation results show (see Figs. 4 and 5) that it is only necessary to have 3-4 iteration cycles to converge to the optimum design state; the flutter speed rose 13.6%, the weight increased 3.75%; the aileron efficiency rose 275% and the weight increased 14%. Synthetic optimization results show (see Fig. 7) that it is only necessary to use two iteration cycles to reach the synthetic optimization state, the main constraint is the aileron efficiency constraint and aside from the root being the "minimum dimension element" and "stress critical element", all of the others are "aileron efficiency critical elements". The trailing edge skin of the aileron area and its inner side (5,9 element linking) has the most noteable effects on aileron efficiency. The thickness of the "stress critical elements" 6,13 and 14 are all reduced as compared with the thickness during the first full stress. This is due to the increases of the thicknesses of the other element linkings which causes rematching of the inner force. Synthetic optimization results also show that on the basis of full stress, we must cause the K value to rise from 0.088 to 0.3 (increase of 240%) which requires increasing the weight 69.5 kilograms (increase of 15.4%); at the same time, the flutter speed rises from 485 meters/second to 592 meters/second (increase of 22%). We can see from this that for the wing surface structural design of modern fighters, it is necessary to simultaneously consider the requirements of aeroelasticity and static strength.

VI. Concluding Remarks

The SAFDOP system provides a feasible method for synthetic optimization calculations of the wing surface structure. After several iteration cycles, we can reach the goal of an approximate minimum weight design, yet it is also necessary to make further developments and improvements so as to adapt to the needs of the synthetic optimum design of composite material wing surface structures.

The SAFDOP system computer program of optimum design of a wing surface structure with multiple constraints was jointly completed by Lin Liang, Guo Feng, Wang Shihao, Zhang Yining, Sun Qishan, Ba Hengyu and Yao Guijun. We also received the guidance of high level engineer comrade Guan De.

References

[1] Li Liang, Guo Feng and Xie Tianzhen, "Optimum design of aircraft wing surface structures (full stress method)", Aviation Science and Technology, 1981.1.

[2] Sun Qishan, Guo Chunpu, Pan Yixin, Chu Mingjin and Zhang Yining, "On the optimum design program of the wing structure requiring flutter and its applications", Aviation Science and Technology, 1981.1.

[3] Kieth Wilkinson, Joel Markowitz, Edwin Lerner and Dino George, "FASTOP: A flutter and strength optimization

program for lifting-surface structures", Journal of Aircraft, June 1977.

[4] Gabriel Isakson, Harry Pardo, Edwin Lerner, "ASOP-3: A program for optimum structural design to satisfy strength and deflection constraints", Journal of Aircraft, July 1978.

[5] Edwin Lerner and Joel Markowitz, "An efficient structural resizing procedure for meeting static aeroelastic design objective", Journal of Aircraft, February 1979.

THEORETICAL SPECIFIC IMPULSE FOR TWO-PHASE FLOW IN NOZZLE OF ROCKET-RAMJET ENGINE- A SIMPLE ESTIMATION METHOD

Bi Shiguan

Beijing Research Institute, China Precision Machinery Company

Abstract

This paper derives a theoretical specific impulse formula for two-phase flow in nozzle rocket-ramjet engine on the basis of similarity to that used for rocket engines. Theoretically, it is proved that the properties of two-phase flow in nozzle for these two types of engines can be analyzed with a common combined parameter which is equivalent to the exhaust velocity. We introduce a simple estimation method for specific impulse losses of two-phase flow with variable lag. We propose an approximate solution to deal with the problem of singularity.

Main Symbols

A : area

a_c : velocity of sound in combustion chamber

C_{pg} : gas air pressure specific heat

C_s : particulate matter specific heat

C_{pM} : two-phase mixture specific heat

d_t : nozzle throat diameter

f_a : resistance correction coefficient

f_n : heat transfer correction coefficient

I_s : specific impulse

$\Delta \bar{I}_s$: $\frac{I_{so}-I_s}{I_{so}}$: relative specific impulse loss

M_0 : Mach number

n : ignition firing mised flow rate ratio

n_g : ignition firing after combustion flow rate ratio

p : pressure

R_g : gas constant

r_p : grain radius
T : temperature
u : velocity
v : specific heat ratio
ρ : density
η_0 : two-phase flow rate ratio
μ_c : gas viscosity coefficient of combustion chamber
$\xi_0=\frac{X}{L}$: relative nozzle length
$K=\left(\frac{C_s}{C_{pMo}}\right)^2$: specific heat coefficient
$\varepsilon_o=\frac{2}{9}\frac{a_c}{\mu_c}\frac{\rho_s}{d_s}r_p^2$: lag characteristic coefficient
$\zeta=\frac{p}{p_c}$: relative pressure ratio
$\omega_u=\frac{u_p}{u_g}$: relative velocity lag quality
$\omega_T=\frac{T_c-T_p}{T_c-T_g}$: relative temperature lag quantity
α : residual air coefficient
β : theoretical air-fuel ratio

Lower Symbols

o : equilibrium quantity without lag
g : gas quantity
p : grain quantity
M : two-phase mixture quantity
c : combustion chamber quantity
s : particulate matter quantity
i : nozzle inlet section quantity
e : nozzle outlet section quantity

I. Use of the Theoretical Specific Impulse Formula For Two-Phase Flow in Nozzle

Based on the two-phase flow theory of solid rocket engines

[1-5], under design conditions, the two-phase flow theoretical specific impulse of the rocket engine nozzle can generally be expressed as follows:

$$I_s = \frac{1+\eta_0\omega_a}{1+\eta_0}\;\frac{u_g}{g} \qquad (1)$$

Can we use a similar method to calculate the theoretical specific impulse of a rocket-ramjet engine nozzle? Truly, in the rocket-ramjet engine, due to the entrance of air, the combustion process of its fuel and the rocket engine have marked differences and each type of rocket-ramjet engine also have differences because of the air permeating into the after combustion. Thus, as regards the flow of the gas flow in the nozzle, because we can always view the gas mixture of the nozzle inlet area as being formed by two-phase material, we should also be able to use a method similar to that for rocket engines to study the problem of its two-phase nozzle flow. In order to not lose universality, we selected the after combustion and completely combined rocket-ramjet engines as the objects of research. Based on the law of the conservation of momentum, after suitable conversion, we can indicate the fuel equivalent theoretical specific impulses of these two types of engine nozzles in the following forms:

After combustion:

$$I_{sM} = \frac{1}{g}\left[(1+n)\frac{1+\eta_{\text{э}M}\omega_{aM}}{1+\eta_{0M}}\,u_{gM} - nu_e\right] \qquad (2)$$

Completely combined:

$$I_{sM} = \frac{1}{g}\left[\left(1+n+\frac{n-n_g}{\alpha\beta}\right)\frac{1+\eta_{\text{э}M}\omega_{aM}}{1+\eta_{0M}}\,u_{gM} - nu_e\right] \qquad (3)$$

It can be known from the above formulas that even though the operating principles of the rocket and rocket-ramjet engines are different and the combined formulas of each type of rocket-ramjet engine are different, yet the rules of the effects of the grains on them are very similar as both are shown by a common combined paramter $\frac{1+\eta_0\omega_u}{1+\eta_0}u_g$. Therefore, we can use the research on this combined parameter to reveal the common effect laws of the two-phase flow effect on the performance of each type of engine. $\frac{1+\eta_0\omega_u}{1+\eta_0}u_g$ can then be viewed as the equivalent outlet exhaust velocity of the nozzle when there is two-phase flow and thus the problem of two-phase nozzle flow specific impulse loss actually becomes the problem of the two-phase nozzle's equivalent outlet exhaust velocity. Its general formula can be expressed as follows:

$$\frac{1+\eta_0\omega_u}{1+\eta_0}u_g=\frac{1+\eta_0\omega_u}{1+\eta_0}\left[2C_{pM}T_c\left(1-\zeta^{\frac{\nu-1}{\nu}}\right)\right]^{1/2} \qquad (4)$$

In the formula

$$\left.\begin{aligned}
C_{pM}&=(G_g+\eta_0\omega_T C_s)/(1+\eta_0\omega_u^2)\\
\nu&=B_r\nu_g/[1+(B_r-1)\nu_g]\\
B_r&=(1+\eta_0\omega_u)\frac{C_{pM}}{C_{pg}}-\eta_0\frac{T_c-T_g}{T_g'}\left[\frac{2(1-\omega_u)\omega_u' C_{pM}+(1+\eta_0\omega_u)\omega_T' C_s}{(1+\eta_0\omega_u^2)C_{pg}}\right]
\end{aligned}\right\} \qquad (5)$$

ω_u', ω_T' and T_g' are separately the differentials of ω_u, ω_T and T_g for ξ_0.

II. Solution of the Equivalent Exhaust Velocity

Aside from the simple two phase flow without lag and with constant lag of $\omega_u' = \omega_T'=0$, in most situations, because of the ω_u and ω_T quantities of the changes produced along the nozzle's axial and radial directions, there is no way of using a simple method for direct solution. There are two main approximate solutions for the variable lag two-phase flow process: one is the analytical method and the other is the numerical value method [6-8]. During rough calculations, we can use the analytical method and although the precision is a bit poor yet it can allow engineers and technicians to directly view the dependent relationship between the various initial parameters which they selected themselves and the calculation results. They can thus clearly know how the selection of parameters can causes the calculation results to face their own hoped for direction changes. When we use the analytical method to find the equivalent exhaust velocity, its formula can be expressed as:

$$\frac{1+\eta_0\omega_s}{1+\eta_0}u_s=u_0\left[1-\epsilon_0\frac{\eta_0}{1+\eta_0}\,\frac{J(\zeta)}{v_0^2M_0^2}\right] \tag{6}$$

In the formula

$$J(\zeta)=\int_{\zeta_i}^{\zeta_e}\frac{1+\frac{f_d}{f_n}\kappa(v_0-1)M_0^2}{M_0}\,\frac{\zeta'}{\zeta^2}d\zeta$$

Under Stokes flow conditions, because $f_d=f_n=1$, we can then further simplify it into:

$$J(\zeta)=\int_{\zeta_i}^{\zeta_e}\frac{1+\kappa(v_0-1)M_0^2}{M_0}\,\frac{\zeta'}{\zeta^2}d\zeta$$

When compared with the two-phase flow without lag, the specific impulse loss created by the lag is expressed by a relative quantity:

$$\Delta\bar{I}_s=\epsilon_0\frac{\eta_0}{1+\eta_0}\,\frac{J(\zeta)}{v_0^2M_{e_0}^2} \tag{7}$$

The above formula shows that the specific impulse loss created by grain lag is not only related to the basic characteristic parameters of η_0, ε_0, v_0 etc. two-phase combustion products, but is also related to the size and change law of the nozzle form's characteristic parameter ζ'.

Thereofre, under two-phase flow, this causes the other conditions to be the same and only because the nozzle forms are different this can in the same way cause the same engine to have different specific impulse losses.

III. Nozzle Form Coefficient

In order to compare the effect of the nozzle forms on the two-phase flow characteristics, we can use a nozzle form coefficient f_z to express the ratio of a common form nozzle's specific impulse loss and the specific impulse loss of the minimum loss nozzle:

$$f_z = \frac{\Delta \bar{I}_s}{\Delta I_{s\,\min}} = \left(\frac{\eta_0}{1+\eta_0}\,\frac{\epsilon_0}{\nu_0^2 M_{e_0}^2}\right) \Big/ \left(\frac{\eta_0}{1+\eta_0}\,\frac{\epsilon_0}{\nu_0^2 M_{e_0}^2}\right)_{\min} \frac{J(\zeta_e)}{J(\zeta_e)_{\min}} \qquad (8)$$

When the operating conditions of the powder charge composition and the engine are the same, the above formula can be simplified into:

$$f_z = J(\zeta_e)/J(\zeta_e)_{\min} \qquad (8a)$$

In the formula

$$J(\zeta_e)_{\min} = C_e^2 \xi_{e_0}$$

$$C_e = \frac{1}{\xi_{e0}} \int_{\zeta_e}^{\zeta_t} \left[\frac{1+\kappa(\nu_0-1)M_e^2}{M_e}\right]^{1/2} \frac{1}{\zeta}\, d\zeta$$

In this way, the effects of the nozzle form can be made to stand alone from the total effeciency of the nozzle and be a single factor for carrying out deeper research. At the same time, we also provide a new method for experimental research on the nozzle form characteristics and comparing the differences between the theoretically calculated results and the test results. Calculations show that the value of common nozzle form coefficient f_z is approximately between 1.5 and 2.5.

IV. An Approximate Solution of the Singularity

Because nozzle form parameter ζ' is a quantity of sinularity existing in the throat, there is generally no way of directly finding its thraot value and thus there is also no way of directly finding the value of arbitrary function integral term $J(\zeta)$. In the references, they proposed an approximate solution of the singularity problem of several types of non-isentropic flows and thus as regards the two-phase nozzle process, some of these solutions are not very suitable while some have relatively low precision. In order to attain simplicity as well as sufficient precision, here we will propose a constant slope method. Its formula is:

or

$$\left.\begin{aligned}\left[\ln\frac{1}{\zeta}\right]'_t&=\left[\ln\frac{1}{\zeta}\right]'_{im}+C_t\left(\ln\frac{1}{\zeta_t}-\ln\frac{1}{\zeta_{im}}\right)\\ \left[\ln\frac{1}{\zeta}\right]'_t&=\left[\ln\frac{1}{\zeta}\right]'_{e_0}-C_t\left(\ln\frac{1}{\zeta_{e_0}}-\ln\frac{1}{\zeta_t}\right)\end{aligned}\right\} \tag{9}$$

In the formula

$$C_t=\left[\left(\ln\frac{1}{\zeta_{e_0}}\right)'-\left(\ln\frac{1}{\zeta_{im}}\right)'\right]\Big/\left(\ln\frac{1}{\zeta_{e0}}-\ln\frac{1}{\zeta_{im}}\right)$$

ζ is the relative pressure value of the nozzle throat area; ζ_{im} and ζ_{e0} are separately the relative pressure values of the upstream and downstream joining point area close to the nozzle throat.

Institute Vice-President Liang Shouban went over this paper and Assistant Head Engineer Bao Keming proposed valuable views for guidance and we would like to express out sincere thanks to them here.

References

[1] W.D. Rannie, A Perturbation Analysis of One-dimensional Heterogeneous Flow in Rocket Nozzle, Detonation and Two-Phase Flow, 1962.

[2] F.E. Marble, Dynamics of a gas containing Small Solid Particle, 5th AGARD Combustion and Propulsion Colloquium, 1963, p175-213.

[3] Solid Rocket Motor Performance Analysis and Prediction, NASA SP-8039, 1971.

[4] Б. В. Орлов, Термодинамические и Баллистические Основы Проектирования Ракетных Двигателей на Твёрдом Топливе, Изд-во «Машиностроение» 1968.

[5] B.V. Orlov, G. Yu. Mazing et al, Design Principles of Rocket-Ramjet Engines for Unmanned Flight Vehicles, Chapter III 3.8 AD 672900.

[6] Benjamin B. Frederik, Two-Phase Nozzle Flow (Gas-Solid), AD 750038, 1972.

[7] D.E. Coats, et al, A Computer for the Prediction of Solid Propellant Rocket Motor Performance, 1975. AD-A01540-42.

[8] M.J. Zucrow and J.D. Hoffman, Flow of Gas-Particle Mixtures, Gas Dynamics Vol. 2, 1976.